Development of Non-Spatial Grid-Like Neural Codes Predicts Inference and Intelligence

Yukun Qu[1,2], Jianxin Ou[1,2], Luoyao Pang[1,2], Shuqi Wu[1,2], Yuejia Luo[1,3], Tim Behrens[4,5,6], Yunzhe Liu[1,2*]

1. State Key Laboratory of Cognitive Neuroscience and Learning, IDG/McGovern Institute for Brain Research, Beijing Normal University, Beijing, China
2. Chinese Institute for Brain Research, Beijing, China
3. School of Psychology, Center for Brain Disorders and Cognitive Science, Shenzhen University, Shenzhen, China
4. Wellcome Centre for Human Neuroimaging, UCL, London, UK
5. Wellcome Centre for Integrative Neuroimaging, University of Oxford, Oxford, UK
6. Sainsbury Wellcome Centre for Neural Circuits and Behaviour, UCL, London, UK

* Correspondence: yunzhe.liu@bnu.edu.cn (Y.L.)

Abstract

Piaget's theory emphasizes children develop structured knowledge schemas for assimilating new concepts, yet the neural mechanisms and their link to intelligence remain unclear. In 203 participants aged 8–25 years, we investigated how maturation of neural representations of a two-dimensional knowledge map supports inferential reasoning and assimilation. We found that grid-cell-like neural codes in the entorhinal cortex (EC) strengthen with age, forming structured representations in non-spatial conceptual spaces. This maturation is directly linked to improved inferential reasoning. These grid-like codes support the medial prefrontal cortex (mPFC) in encoding distance relationships between concepts. As participants assimilated new information, they integrated it into existing grid patterns in the EC. Furthermore, maturation of these neural codes predicts real-world intelligence measures, particularly in abstract reasoning. Our findings show that the development of non-spatial grid-like neural codes underpins inference and knowledge assimilation, providing a neural basis for cognitive development and linking cellular neuroscience with intelligence.

Keywords: cognitive map, development, inference, grid-like code, entorhinal cortex (EC)

Introduction

As we grow older, our understanding of the world deepens. Consider our learning process in school. Initially, we might remember facts as isolated pieces of information. As we mature, we begin to grasp not just the concepts themselves, but also how they are connected and organized into a larger knowledge map. This understanding helps us infer relationships between concepts, even those not directly observed. Ultimately, with this knowledge map, we can assimilate new concepts within the same framework. This structured knowledge, referred to as cognitive map[1] or schema[2,3], undergoes 'intellectual evolution' as we develop from childhood to adulthood[4-7]. This represents a significant underpinning of human cognition[8]. However, the neural mechanism of its development, remains largely unexplored.

There are two ways to develop structured knowledge[9]. The first involves creating links between concepts, allowing us to determine the distance between disjoint concepts when inferring their relationship. This 'distance code' representation, akin to a specific map, can be developed from experiences, such as forming a successor representation[10-12]. Alternatively, one can generalize a common abstract structure from different experiences, resembling a schema[13,14]. In two-dimensional (2D) environments, schema representation is supported by grid cells in the entorhinal cortex (EC). Grid cells fire in hexagonal patterns and generalize the grid pattern across environments[15,16]. This contrasts with the representation by hippocampal place cells, which encode a specific map and undergo remapping in different environments[17]. This applies to both physical space[18] and arbitrary conceptual spaces[19,20]. In cognitive development, for instance, Piaget [4] suggested that children begin to infer transitive rankings between objects around the age of 7 or 8 years. It would be intriguing to explore its neural underpinnings. The question is whether this ability arises because children have constructed a particular sequence of specific objects (i.e., current map representation), or if they have formed a general concept of 'line' (i.e., schema representation).

The two representations are not exclusive. Having a schema, for instance, allows for quicker construction of the current map and enables immediate inference without prior exposure[8]. We are interested in how such neural representations and their consequent

inference ability evolves during development. We use a distance code to investigate map-like representations and a grid-like code for schema representation. If individuals construct their current map based on the schema, we expect to see a significant influence of the grid-like code on the distance code.

When a schema is established, the process of assimilating new knowledge changes. Instead of creating a new map, one can make local adjustments to the existing one. This assimilation mechanism begins in childhood and persists throughout life, facilitating the ongoing development of cognition[21]. Animal studies have shown that the medial prefrontal cortex (mPFC) is crucial in linking new sensory cues to specific locations within known environments, enabling rapid assimilation[22]. In such instances, the representation of the existing schema should be maintained. In the current study, we explore how the assimilation of new knowledge develops with age, particularly once a conceptual schema has been formed. This question is intriguing because the mPFC, which continues to develop into adulthood[23,24], is thought to play a key role in the accumulation of knowledge[25,26]. We expect that this assimilation depends on how well the new information aligns with the existing schema representation, and that the mPFC plays an age-dependent role.

Results

Age-related improvement in inferential reasoning and new knowledge assimilation

We recruited 231 participants aged 8–25 years, ensuring that each age year included at least ten subjects (see Methods and **Extended Data Table 1**). Before the main experiment, participants memorised the rank differences between 25 objects, each characterised by two independent attributes: attack power (AP) and defence power (DP). Unbeknownst to them, these objects were organised into a 2D map with five ranks in each dimension. Participants learnt only the rank differences between neighbouring objects within each dimension, without knowledge of the underlying 2D structure. During fMRI scanning, they were required to infer relationships between objects across both dimensions, effectively navigating a 2D knowledge map (**Fig. 1a**).

In the memory training phase, participants engaged in "piecemeal learning," where they learnt relationships between objects differing by one rank in each dimension, presented in random order (see Methods). They were informed that one-rank differences were equidistant but were not told about the underlying 2D map. This training phase could take place over multiple days. Only participants who consistently achieved at least 80% accuracy were invited to the fMRI experiment, ensuring that all participants had sufficient experience to potentially construct a mental 2D map.

Three days before the formal fMRI experiment, participants reviewed all the pairs they had learnt. A knowledge retention test (without feedback) was conducted shortly before the fMRI scanning session on the same day. Only those who achieved at least 80% accuracy proceeded to the fMRI experiment. Their memory performance as a function of age is shown in **Fig. 1c**.

To ensure that younger participants (under 12 years old) were comfortable with the scanning environment, they underwent a mock MRI session before the actual fMRI experiment (see Methods). All participants received clear instructions about the tasks and were asked to confirm their understanding before entering the scanner. We also verified through post-scan debriefings that every subject, including the youngest, understood the tasks. This ensured that all participants performed the tasks as intended.

During the fMRI experiment, participants faced novel inference questions requiring knowledge from both dimensions, termed "map-based inference" or "Game 1." In each trial, they viewed two objects sequentially and recalled their attributes across both dimensions. After a short delay, they were presented with a decision rule and asked to compare the attack power of one object against the defence power of another to determine the winner (**Fig. 1b**; see Methods for details). If participants successfully structured their existing knowledge into a five-by-five 2D knowledge map, each inference trial would resemble navigating a mental map.

After excluding participants who failed learning and memory tests or had excessive head movement during scanning (mean framewise displacement > 0.2 mm), 203 participants were included in the final analysis. Following the map-based inference phase, we introduced four new objects at the centre of the map. Participants then learnt the relative rank differences between these new objects and their immediate neighbours—a phase called "local learning." They used the same procedure as in the earlier training and were informed that the relationships between existing objects would remain unchanged.

The aim was to ensure that all participants, regardless of age, could adequately learn the local associations before proceeding to the non-local inference task. If they successfully assimilated this new knowledge into the existing map, they could make "nonlocal" inferences between the new objects and distant existing ones, termed "Game 2" or "nonlocal inference." Of the 203 participants, 193 completed Game 2 and provided usable fMRI data.

To validate our task design in capturing age-related development in structured knowledge, we used inferential reasoning and assimilation ability as its behavioural indices. We first analysed behavioural performance during both Game 1 and Game 2. During the piecemeal learning phase, we observed a positive correlation between age and memory performance ($r = 0.19$, $p = 0.01$, $N = 203$; **Fig. 1c**). More importantly, there was a strong age effect on map-based inference performance in Game 1 ($r = 0.56$, $p < 0.001$; **Fig. 1d**), which remained significant after adjusting for memory differences ($r = 0.54$, $p < 0.001$). These results suggest an age-related developmental effect on inferential reasoning, above and beyond memory capacity.

A similar pattern was observed for nonlocal inference ability in Game 2 ($r = 0.56$, $p < 0.001$; adjusted for memory: $r = 0.54$, $p < 0.001$, $N = 193$; **Fig. 1e**). Linear regression analysis corroborated these findings. The model revealed a significant effect of age on nonlocal inference performance ($t(188) = 2.02$, $p = 0.04$, Cohen's $d = 0.10$), while memory performance during learning did not (training memory: $t(188) = –0.35$, $p = 0.73$, Cohen's $d = –0.01$; new knowledge memory: $t(188) = 1.47$, $p = 0.14$, Cohen's $d = 0.07$). Notably, the age effect on Game 2 performance persisted even after controlling for Game 1 performance ($r = 0.17$, $p = 0.02$; **Fig. 1f**). These results suggest a unique developmental effect of assimilating new information, beyond just existing map knowledge.

To ensure that the age-related effect was not due to younger subjects being unable to perform the task, we confined our analysis to subjects under 12 years old and found they performed significantly above chance on all tasks (map-based inference: $t = 12.46$, $p < 0.001$; nonlocal inference: $t = 11.01$, $p < 0.001$).

To confirm that the age-related increase in inference ability was not simply due to differences in memory capacity, we conducted further supplementary analysis excluding inference trials involving objects that were incorrectly identified in the memory test. The age-related improvement in map-based inference remained significant ($r = 0.51$, $p < 0.001$).

We also conducted extensive analyses to rule out potential age-related confounding factors such as sampling biases, forgetting, and participant fatigue, none of which explained the observed age-related increase in inferential ability (see **Supplementary Note 1**).

Overall, these results highlight the age-dependent development of inferential reasoning and assimilation abilities, demonstrating that age has a selective impact on abstracting knowledge structure and integrating new information into existing knowledge structures.

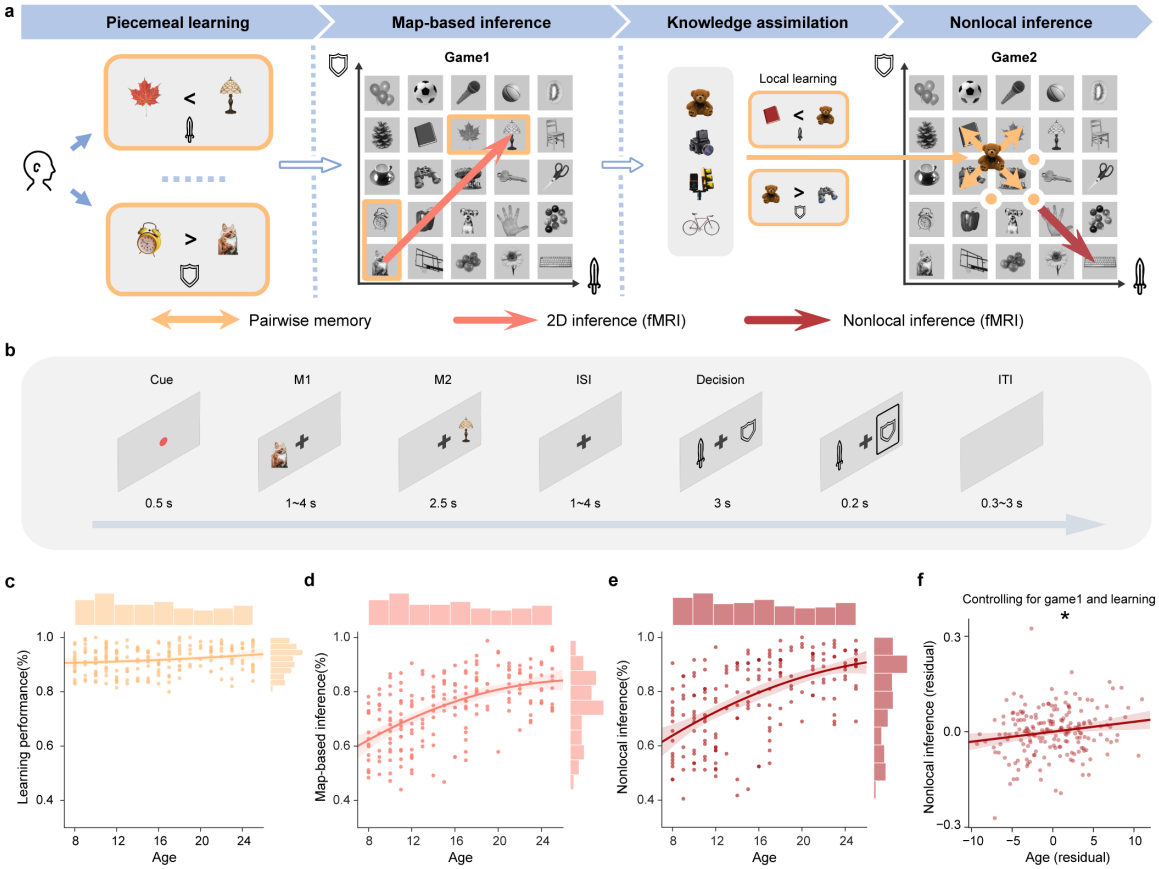

Fig. 1 | Experimental design and age-related increase of novel inference ability based on cognitive map. a, A knowledge map serves as a type of cognitive map. In this study, the map is based on two independent dimensions: attack power (AP) and defence power (DP). It comprises 25 distinct objects (referred to as "monsters" in the cover story), each characterized by these two features. During the memory training phase, subjects were exposed to neighbouring relationships of objects within a single dimension (yellow rectangle), without knowing the latent structure of the two-dimensional (2D) map. Only those who achieved an 80% accuracy in this piecemeal learning phase advanced to the map-based inference task, which was conducted alongside fMRI scanning. This fMRI task required participants to consider both dimensions and infer relationships between novel object pairs (indicated by red arrows), termed map-based inference. It contained 252 trials covering all possible trajectory directions on the map, also referred to as Game1. Following Game1, participants encountered four new objects placed at the map's centre (e.g., the "bear" and three orange points). They first learnt the relationships between these new objects and their neighbouring existing ones (indicated by yellow arrows). Subsequently, they were tasked with making non-local inferences between the new objects and distant existing ones (dark red arrow). This phase is termed Game2 to differentiate it from Game1. Game2 primarily tests the ability to assimilate new knowledge using the existing map. **b,** In each trial, Monster1 (M1) and Monster2 (M2), followed by the fighting rule, are displayed sequentially. Participants must recall each monster's two attributes and then compare the attacker's AP to the defender's DP to identify the higher-ranked monster. The roles of attacker and defender are only clarified during the decision time based on the revealed fighting rule. As this rule changes randomly across trials, it prompts subjects to separate mental navigation from the decision-making process (see also **Extended Data Fig. 3**). **c-e,**

Developmental changes of behavioural performance, separately for piecemeal learning (**c**), map-based inference (or Game1) (**d**), and non-local inference based on new knowledge (or Game2) (**e**). **f,** After further controlling for learning performance and Game1 inference ability, a positive correlation between Game2 inference ability and age still existed. Each circle denotes data from individual subject. Error bars denote s.e.m. *: $p < 0.05$.

Development of grid-like code in the EC enhances inferential reasoning

We aimed to uncover the neural basis underlying the development of structured knowledge and its resulting flexible behaviour. First, we want to know whether the grid-like code[15,18], a cellular mechanism for representing schemas in 2D spaces, also exists in representing knowledge map and how it evolves with age to support inferential reasoning abilities.

To this end, we employed three established methods in fMRI for detecting grid-like code. These are: a) hexagonal modulation analysis[20,27]; b) hexagonal consistency analysis[18-20]; and c) representation similarity analysis (RSA) of angular difference between inferred trajectories[28]. All these approaches aim to detect the alignment between neural signals and grid angle. This alignment is specific to a six-fold or hexagonal symmetry (**Fig. 2a**).

Across all three methods, we consistently identified significant grid-like code in the EC (**Fig. 2b**; whole-brain cluster-based family-wise error (FWE) correction at $p < 0.05$; hexagonal modulation effect: peak $z = 5.48$, MNI coordinate [-20, 1, -34], consistency effect: peak $z = 4.69$, MNI coordinate [-28, 3, -38], left panel; and representation similarity: peak $z = 4.93$, MNI coordinate [-28, -2, -42], right panel, also see **Extended Data Fig. 1** and **Supplementary Table 1**). To visualize the hexagonal activation pattern, we grouped all inferred trajectories into 12 bins based on their angle directions relative to the grid angle (**Fig. 2c**). Neural activity for aligned trajectories in the EC anatomical ROI[29] was significantly higher than for misaligned trajectories (paired-*t* test, $t(74) = 10.15$, $p < 0.001$, Cohen's $d = 2.34$; **Fig. 2d**). Notably, this consistency effect was significant only for six-fold symmetry (one-sample *t* test, $t(74) = 3.12$, $p = 0.003$, Cohen's $d = 0.36$), not for 4, 5, 7, or 8-fold periodicities (**Fig. 2d**).

After identifying the grid-like code on the 2D knowledge map across subjects, we further examined its relationship with age and cognitive map-based inference. The grid-like code was measured using RSA, which does not require estimating the ROI-specific mean orientation[28]. A whole-brain covariate analysis revealed an increase in the grid-like code in EC with both inference performance and age (age: peak $z = 2.70$, MNI coordinate [-32, -16, -28]; inference: peak $z = 4.72$, MNI coordinate [27, -10, -28]; **Fig. 2e**). Further ROI

analysis on EC supported these findings (inference: $r = 0.31$, $p < 0.001$; age: $r = 0.16$, $p = 0.02$, **Fig. 2f**).

To verify the robustness of the observed age-related increase in grid-like code in the EC, we conducted several control analyses. First, we examined whether the correlation between grid-like code and age could be attributed to general changes in the signal-to-noise ratio (SNR) in the EC with age. Our analyses revealed no significant relationship between age and SNR in the EC (Game 1: $r = -0.09$, $p = 0.19$; Game2: $r = -0.06$, $p = 0.38$; see **Supplementary Note 2**), indicating that the observed effects are not due to SNR differences across ages.

Next, to rule out systematic differences between adults and children, we repeated the analysis focusing solely on participants under 18 years old. We found that the grid-like code in the EC still significantly correlated with both inferential performance ($r = 0.35$, $p < 0.001$) and age ($r = 0.18$, $p = 0.04$). Furthermore, when we examined more fine-grained age differences, we discovered that the relationship between grid-like code and improved inference performance was strongest in children aged 8 to 12 years ($r = 0.32$, $p = 0.004$).

These findings suggest that the development of grid-like code in the EC plays a crucial role in enhancing inferential abilities. To directly test this, we conducted a mediation analysis, which showed that the increase in inferential ability was mediated by the development of grid-like code (mediation effect: $\beta_{ab} = 0.04$, $p = 0.03$, CI [0.01, 0.08]; **Fig. 2g**). This mediation effect remained significant even after controlling for socioeconomic status (βab = 0.06, $p = 0.02$, CI [0.01, 015], see also **Supplementary Note 1**).

Together, these findings demonstrate that grid-like code in the EC represents the 2D knowledge map. As individuals mature, these grid-like codes become stronger, underpinning the increase in inferential abilities.

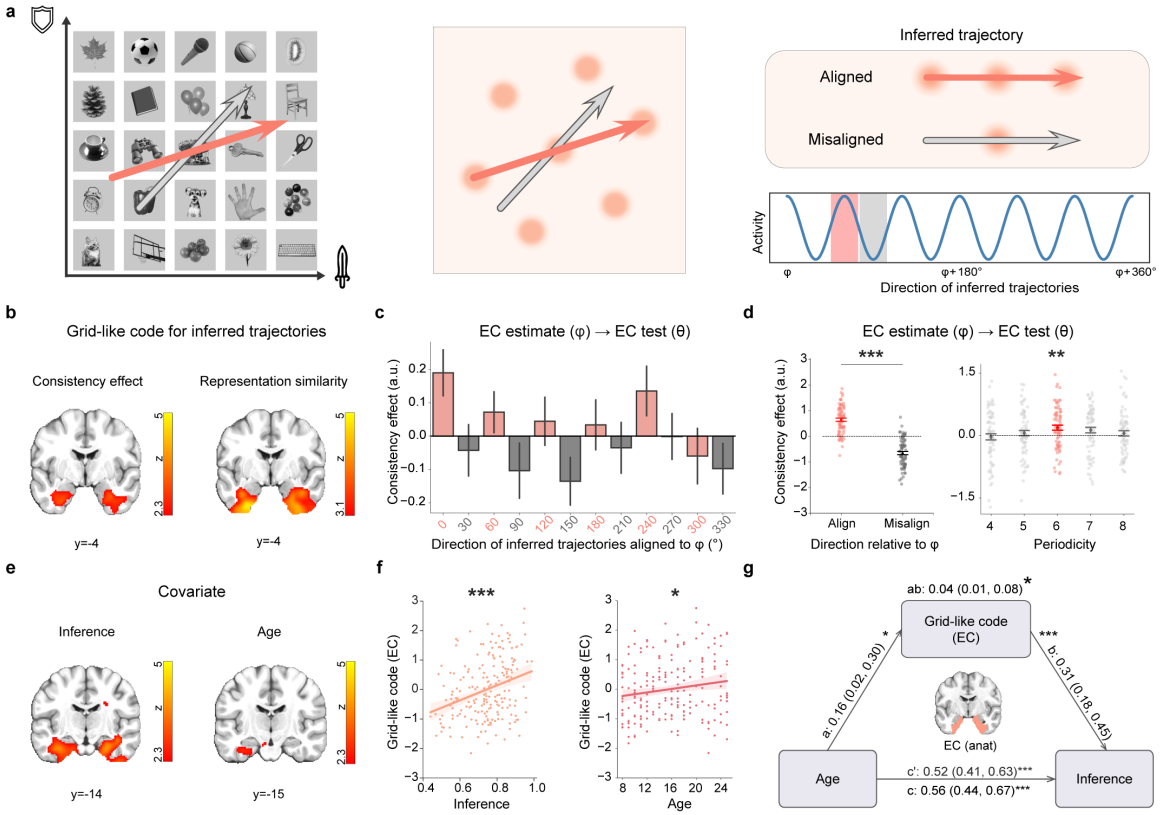

Fig. 2 | Grid-like code in the entorhinal cortex supports age-related increase of inferential reasoning on a 2D map. a, Illustration of the hexagonal pattern of grid-like code. Inferred trajectories traverse both the knowledge map and the firing fields of grid cells. When an inferred trajectory's direction (θ) aligns with the mean orientation (φ) of these grid cells, it intersects more grid fields, which result in increased neural activity compared to misaligned trajectories. This is termed the grid-like code and can be measured in fMRI signal[18,20]. **b**, Grid-like code for inferred trajectories was found in the entorhinal cortex (EC) using either univariate parametric analysis[19] (left) or multivariate representation similarity analysis (right)[28]. These results were observed in participants with high inference performance (accuracy > 0.8; N = 75, see also the **Extended Data Fig. 1**). **c**, The inferred trajectory (θ) in the EC exhibits a six-fold modulation aligned to the mean orientation (φ). Effects are plotted separately for aligned (red) and misaligned (grey) trajectories. **d**, Left panel: A significant difference is observed when comparing the neural activity of aligned trajectories to that of misaligned trajectories. Right panel: The six-fold modulation, when aligned to φ, is specific to a six-fold pattern and not observed for other control periodicities. **e**, In the whole-brain covariate analysis, age and inference performance were incorporated separately, as second-level covariates with the grid-like code. Analysis highlighted a positive effect for both covariates in the EC. For visualization purpose, whole-brain maps were thresholded at $p < 0.01$, uncorrected. **f,** ROI analysis of grid-like code in the anatomically defined bilateral EC (as illustrated in **g**) with inference performance or age. **g,** Mediation analysis suggests that with increasing age, there was stronger grid-like code in the entorhinal cortex, supporting the age-dependent increase of inferential reasoning. Statistical inferences were derived using bootstrapping, with 10,000 iterations, and paths were labelled with coefficients and confidence intervals. Each circle is data from individual subject. Error bars denote s.e.m. *: $p < 0.05$. **: $p < 0.01$. ***: $p < 0.001$.

Development of EC grid-like code supports distance code in the mPFC

Having identified the schema representation (grid-like code) in the EC, we next investigated the map-like representation (distance code) in the mPFC and its relationship with the schema. The distance code represents the Euclidean distances between objects in the map and has been previously identified in the in the mPFC[19,30,31].

During the mental navigation phase (when the second object, M2, appears), we estimated the Euclidean distance between inferred object pairs (**Fig. 3a**). Crucially, if the current map representation is constructed based on the schema, we expect the grid-like code to influence the distance code.

Across all subjects, we found significant mPFC involvement in representing the distance code (whole-brain cluster-based FWE correction at $p < 0.05$, peak $z = 6.23$, MNI coordinate [7, 47, 23]; **Fig. 3b**, upper panel), along with hippocampus, LOFC and PCC at whole-brain level (see also **Supplementary Table 2**). The whole-brain covariate analysis of the distance code with age also indicated a positive correlation in the mPFC (peak $z = 4.30$, MNI coordinate [5, 57, -2]; **Fig. 3b**, bottom panel). At the ROI level, the mPFC was defined independently using an mPFC mask from NeuroVault (see Methods for details). It was also depicted in pink mask in **Fig. 3h**. Notably, the mPFC encoded more of the Euclidean distance in the 2D knowledge map than a one-dimensional hierarchy (paired t-test, $t(202) = 2.69$, $p = 0.008$, Cohen's $d = 0.15$; **Fig. 3c**). This aligns with previous literature suggesting that the mPFC integrates two-dimensional information, rather than representing each dimension separately[27].

Next, we determined whether subjects built the map-like representation based on the schema (see also **Supplementary Note 3** for schematic illustrations distinguishing between schema and map). We categorized all trials as 'aligned' or 'misaligned' based on their angle relative to the mean orientation estimated from the EC. At the whole-brain level, we observed a stronger distance code for aligned trials compared to misaligned trials, with only the mPFC surviving the whole-brain correction (peak $z = 3.57$, MNI coordinate [0, 33, 11]; **Fig. 3e**). ROI analysis further supported these findings (All subjects: $t(202) = 1.95$, $p = 0.03$, Cohen's $d = 0.15$; high performance subjects: $t(74) = 2.72$, $p = 0.004$, Cohen's $d =$

0.22, paired *t* test; **Fig. 3f**; see also **Extended Data Fig. 2**). The results indicate a consistent relationship between the EC grid-like code and the mPFC distance code, and suggest the map-like representation is built based on the schema representation.

Finally, we explored the role mPFC in the age-related increase of cognitive map-based inference, particularly in relation to the EC grid-like code. The strength of mPFC distance code correlated positively with both age (r = 0.24, p < 0.001, **Fig. 3d**) and inference performance (r = 0.23, p < 0.001). There was also a significant mediation effect of the distance code on age-related inference improvement (β_{ab} = 0.03, p = 0.04, CI [0.002, 0.067], **Fig. 3g**, left panel). However, when considering both the EC grid-like code and the mPFC distance code in a parallel mediation analysis[32], only the EC effect remained significant (EC, β_{ab} = 0.04, p = 0.03, CI [0.006, 0.082]; mPFC, β_{ab} = 0.02, p = 0.12, CI [-0.002, 0.057]; **Fig. 3g**, right panel). Further tests confirmed a significant mediation effect of the EC grid-like code on the mPFC influence on inference (β_{ab} = 0.04, p = 0.04, CI [0.004, 0.098]; **Fig. 3h**).

All these effects were specific to the mental navigation when mPFC representing the distance code, rather than the decision time (**Extended Data Fig. 3**; see also **Supplementary Note 4**, **Supplementary Table 3**). Together, these results indicate subjects built the current map representation based on the schema, and the development of the schema (grid-like code) supports the map-like representation (distance code).

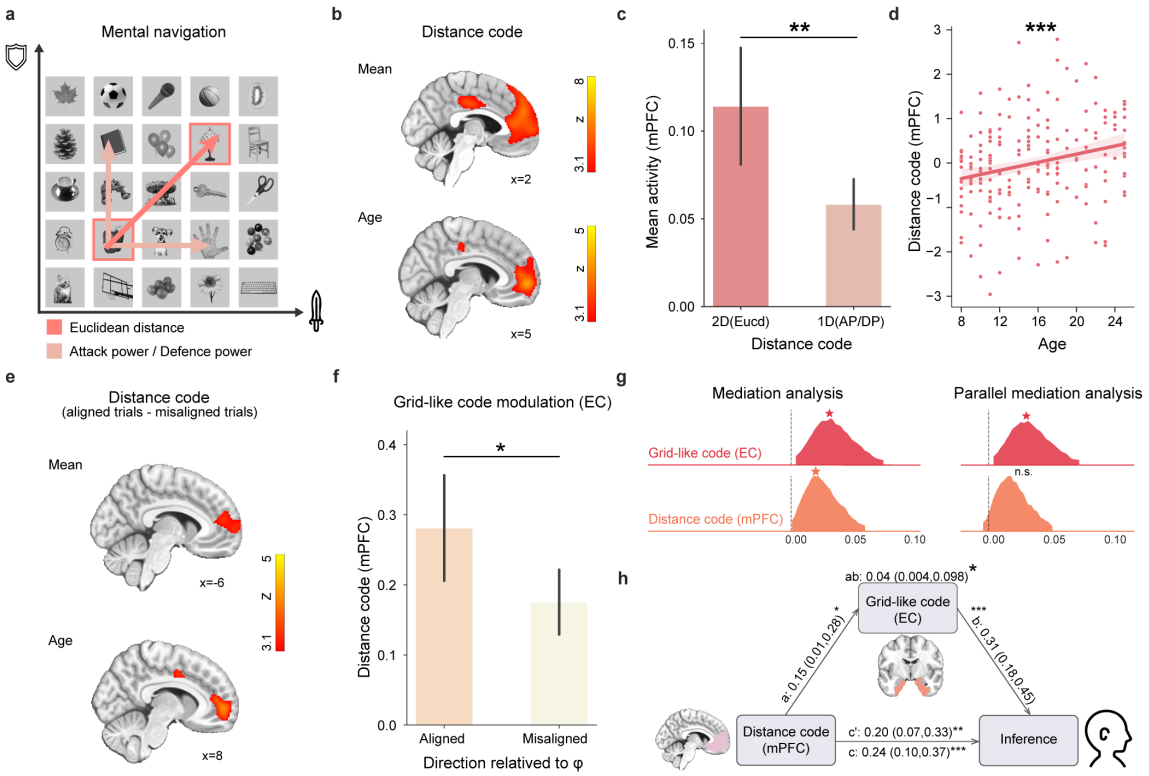

Fig. 3 | Development of the grid-like code in the entorhinal cortex supports the map-based distance code in the medial prefrontal cortex. **a**. An example trajectory (e.g., paprika → lamp) traverses the knowledge map during mental navigation (when M2 appears). To detect the map-like representation between concepts, we calculate their Euclidean distance (red arrow). This distance code integrates inferred relationships across both dimensions, extending beyond a single dimension (light pink arrow). **b**. Whole-brain analysis showed significant mPFC activation encoding the Euclidean distance (top panel) and an age-related increase in the distance code within the mPFC (bottom panel). **c.** ROI analysis in the mPFC revealed stronger coding for the 2D map Euclidean distance than for a single dimension distance (see also **Extended Data Fig. 2 & 3**). **d.** The distance code in the mPFC positively correlated with age. **e.** Whole-brain modulation of the EC grid-like code on the distance code showed significant mPFC activation for the contrast of distance code between aligned vs. misaligned trials (top panel), which also increased with age (bottom panel). Alignment is determined when the direction of the inferred trajectory, θ, deviates by less than 15° from the estimated mean orientation, φ, in the EC. A deviation greater than 15° is considered misalignment. **f.** ROI analysis in the mPFC showed stronger distance code during aligned trials compared to misaligned ones. **g.** Mediation effects of task-related neural activities on the age and behaviour relationship. The dotted line represents zero. Mediation effects was significant when bootstrap confidence intervals exclude zero. **h**. Further analysis indicated that the EC grid-like code mediated the mPFC distance code on the inference performance. Statistical inferences used bootstrapping with 10,000 iterations, and paths were labelled with coefficients and confidence intervals. All brain maps were whole-brain FWE corrected at the cluster level ($p < 0.05$) with a cluster-forming voxel threshold of $p < 0.001$. Each circle is data from individual subject. Error bars denote s.e.m. *: $p < 0.05$. **: $p < 0.01$. ***: $p < 0.001$. n.s. non-significant.

Consistency in the grid-like code facilitates knowledge assimilation

After completing the main inference task, subjects were introduced to four new objects placed at the centre of the original map. They learnt the rank relationships between these new objects and their surroundings on the map. Subsequently, subjects were asked to make novel inferences between these new objects and the existing, distal ones – a process we refer to as nonlocal inference, or Game2 (details in Methods). It is important to note that the structure of the map, and therefore also the schema, remained constant across both inference tasks. If subjects successfully integrated the local changes into the existing schema (as depicted in **Fig. 4a; Supplementary Note 5**), they should be able to perform well on the nonlocal inference. To explore this, we analysed whether the grid-like code generalized and remained consistent after the introduction of the new objects.

In Game2, we first replicated the grid analysis (**Extended Data Fig. 4**, see also **Supplementary Note 6**). We identified significant grid-like code in brain areas such as the EC (peak z = 3.75, MNI coordinate [19, -10, -32]), mPFC (peak z = 4.10, MNI coordinate [-4, 21, -6]), LOFC (peak z = 4.31, MNI coordinate [15, 21, -26]) and PCC (peak z = 3.9, MNI coordinate [1, -44, 27], also see **Extended Data Fig. 5** and **Supplementary Table 4**, surviving whole-brain correction (cluster-based FWE corrected at $p < 0.05$). These areas aligned with those where we previously detected grid-like code in Game1 (also see **Extended Data Fig. 1a**). We then conducted a conjunction analysis comparing the grid-like code between the original and the knowledge-assimilated maps. At the whole-brain level, we found a significant cluster in the right EC (**Fig. 4b**), surviving correction for multiple comparisons ($p < 0.05$, see details in methods). These results indicate that subjects have maintained the consistent schema representation after assimilating new knowledge.

We further assessed the alignment of the grid-like code between the two maps. We estimated the consistency effect by estimating the grid angle from the EC in Game1 and testing its alignment with inferred trajectories in Game2 (see details in methods). A significant map-alignment effect was identified in the EC, which correlated positively with nonlocal inference performance (whole-brain cluster-based FWE correction at $p < 0.05$, peak z = 4.32, MNI coordinate [29, 0, -42], **Fig. 4c**), even after controlling for age differences. ROI analysis of EC revealed its map-alignment strength positively predicted

nonlocal inference performance (r = 0.21, p = 0.003) but was unrelated to age (r = 0.01, p = 0.94, **Fig. 4d**). These results imply that participants who retained a consistent schema were successful in integrating new knowledge for making novel inferences.

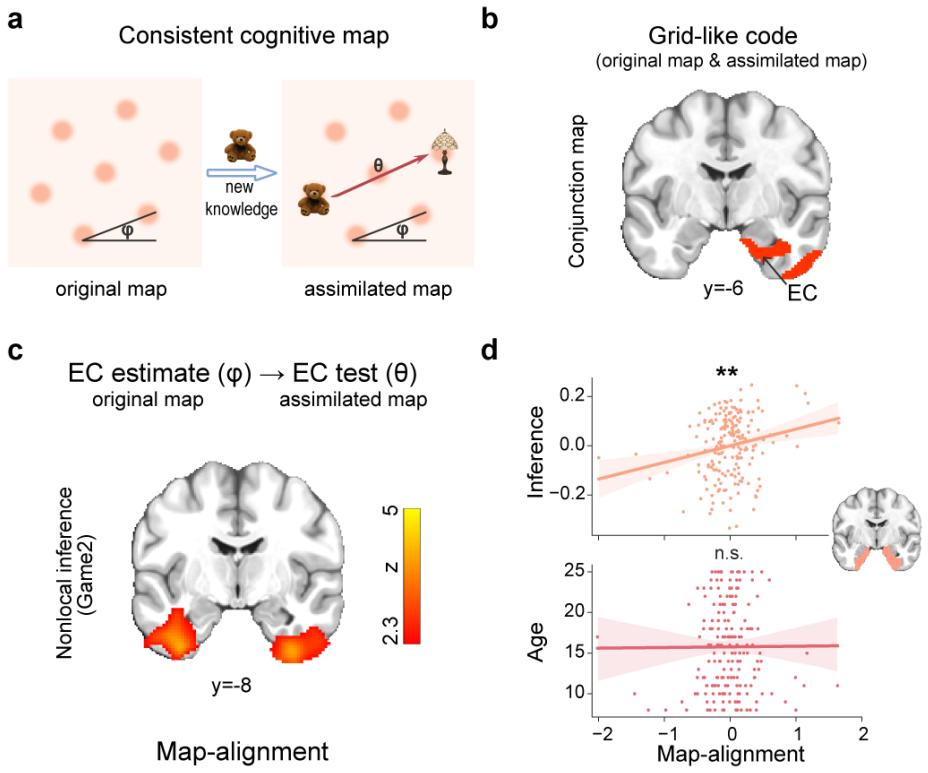

Fig. 4 | Consistency in EC grid-like code facilitates nonlocal inference on a new map. a, If the schema is used to assimilate new knowledge, consistent grid angles (φ) are expected between the original and the new maps. The neural activation of inferred trajectories (θ) on new objects should align with the grid angle of the original map. **b**, Whole-brain conjunction analysis of the grid-like code between the original map (Game1) and the knowledge-assimilated map (Game2). This revealed a significant conjunction cluster in the right EC. **c**, To identify the alignment between the two maps, we compared the neural signal of inferred trajectories on the new map (Game2) to the estimated EC grid angle from the original map (Game1). We found significant clusters in the EC that predict nonlocal inference performance, controlling for age differences. The brain map was whole-brain FWE corrected at the cluster level (p < 0.05) with a cluster-forming voxel threshold of p < 0.01. **d,** ROI analysis of EC revealed that its map-alignment strength positively predicted nonlocal inference performance but was unrelated to age. Each circle is data from individual subject. **: p < 0.01. n.s. non-significant.

mPFC distance code selectively supports age-related development of knowledge assimilation

After identifying a consistent schema representation across maps, we next asked how the current map representation adapts to new information. Tse *et al.* [22] suggest that forming links between new information and existing environments facilitates rapid integration into the spatial schema, and the mPFC is essential in this process. We expect that the new map representation in the mPFC is also important for the assimilation of new knowledge. This is especially significant given the late maturation period of human mPFC[23,24], which implies its ability to facilitate assimilation also evolve through development.

In Game2, we observed a similar and significant distance code in the mPFC (peak $z = 7.13$, MNI coordinate [-8, 55, 3], **Fig. 5a**, left panel), as well as hippocampus, LOFC and the PCC (**Supplementary Table 5**). These findings survived whole-brain correction (cluster-based FWE corrected at $p < 0.05$). A conjunction analysis of the distance code between the original and new map also revealed a significant cluster in mPFC (**Fig. 5a**, right panel). The involvement of the mPFC during Game2 was consistently observed in the whole-brain covariate analysis with both age (peak $z = 6.41$, MNI coordinate [-4, 39, -9]) and nonlocal inference performance (peak $z = 7.69$, MNI coordinate [3, 33, -12], **Fig. 5a**, bottom panel). Similarly to the distance code in Game1, the distance code in the mPFC from Game2 was also modulated by the EC grid-like code, with stronger activation in aligned trials compared to misaligned trials (paired t test, $t(192) = 4.14$, $p < 0.001$, Cohen's $d = 0.23$, see **Extended Data Fig. 6**).

After identifying a consistent map representation across both games, we proceeded to explore whether the ability to assimilate new knowledge into a cognitive map is different from forming a cognitive map, and how this capability develops with age. Incorporating Game1 performance as a covariate, we continued to observe the involvement of the mPFC, correlating with age and Game2 nonlocal inference (**Fig. 5b** upper panel). This correlation was confirmed at the ROI level (age: $r = 0.21$, $p = 0.003$, inference: $r = 0.16$, $p = 0.02$; **Fig. 5b** bottom panel). Mediation analysis showed that, even after controlling for Game1, the mPFC distance code still mediated the age-related increase in nonlocal inference for Game2 ($\beta_{ab} = 0.02$, $p = 0.04$, CI [0.002, 0.042], **Fig. 5c**). Intriguingly, this was not the case

for grid-like code. These indicate the ability of building new map representation in mPFC depends on age and supports rapid assimilation of new knowledge. It also suggests that an additional age-dependent mechanism for assimilating knowledge exists in mPFC on top of the EC grid signal.

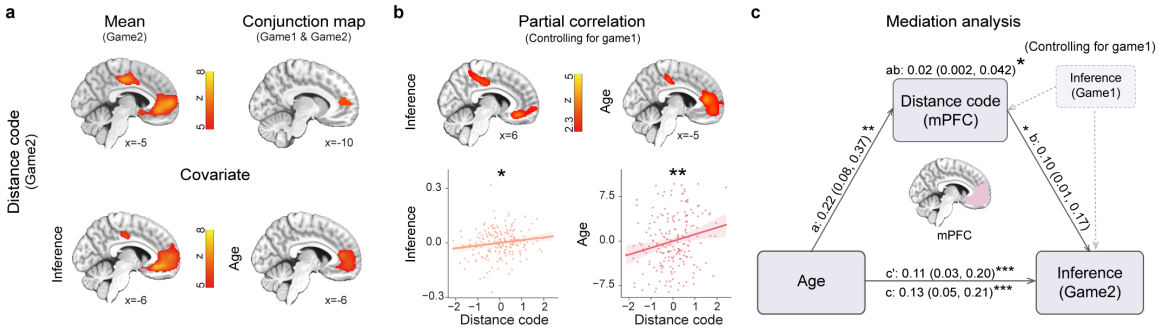

Fig. 5 | mPFC distance code selectively supports age-related development of nonlocal inference. a, Whole-brain analysis revealed significant activity in mPFC encoding the Euclidean distance related to new knowledge in Game2 (panel in top left). A conjunction analysis with the same effect in Game1 also showed overlapping activity in the mPFC (panel in top right). Whole-brain covariate analysis using age or inference performance revealed consistent involvement of mPFC during Game2 (bottom panel). The brain maps survived whole-brain FWE corrected at the cluster level ($p < 0.05$) with a cluster-forming voxel threshold of $p < 0.001$ (see also the **Extended Data Fig. 6**). **b,** Whole-brain covariate analysis and ROI analysis of mPFC found its distance code strength positively correlated with nonlocal inference performance (left) and age (right), controlling for performance differences in Game1. For visualization purpose, the whole-brain covariate maps were thresholded at $p < 0.01$, uncorrected. **c,** Mediation analysis indicated that the distance code in the mPFC mediated the impact of age on nonlocal inference during Game2, even after controlling for inference performance in Game1. Statistical inferences were derived using bootstrapping with 10,000 iterations, and paths were labelled with coefficients and confidence intervals. Each dot is data from individual subject. *: $p < 0.05$. **: $p < 0.01$. ***: $p < 0.001$.

Structural basis of cognitive map through development

Brain structure also evolves significantly during development [23], and this structural change is linked to an increase in inference ability[6]. We aimed to understand the structural basis of cognitive map development, and its relationship with the functional representation of cognitive map during inference task. To this end, we examined developmental changes in both the grey-matter structure and white-matter connectivity of the brain (see details in Methods), as well as their associations with the inferential ability based on the cognitive map.

Using structural MRI (see Methods), we measured grey matter volume (GMV) and thickness to indicate cortical morphometry[33-35]. The total cortical GMV of our subjects decreased from ages 8 to 25, aligning with the developmental trajectory depicted in the human "brain chart"[23] (**Fig. 6a**). Interestingly, while this decreasing trend was observed at the whole-brain level, the GMV in the EC continued to increase in line with age and inference ability from 8 to 25 years old (**Fig. 6b**).

Focusing on EC and mPFC (same definition as in fMRI), both regions exhibited significant correlations with age and inferential behaviour, but they differed in their developmental trajectories in GMV (age: r_{EC} = 0.36, p < 0.001, r_{mPFC} = -0.68, p < 0.001; inference: r_{EC} = 0.21, p = 0.004, r_{mPFC} = -0.38, p < 0.001, **Fig. 6c**). We confirmed that these structural results were consistent across different parcellation methods (see **Supplementary Note 7**), indicating that the observed developmental trends are genuine and not artefacts of any specific atlas. Similar patterns were observed for cortical thickness (**Extended Data Fig. 7**).

Furthermore, we found a significant negative correlation in the mPFC between GMV and the cognitive map representation on-task (distance code) in both Game1 (r = -0.23, p < 0.001 and Game2 (r = -0.36, p < 0.001). No significant connections were found in EC between its structural changes and grid-like code. Mediation analysis indicated that age-related structural changes in the mPFC influenced its task representation of the cognitive map (β_{ab} = -0.21, p < 0.001, CI [-0.34, -0.10], **Fig. 6d**).

Using diffusion MRI (see Methods), we also measured the structural connectivity in the brain, focusing on the mean fractional anisotropy (FA) of white matter tracts[36]. This approach revealed that the tracts between the EC and mPFC had the most pronounced age-related changes and were significantly correlated with inference performance (age: $r = 0.48$, $p < 0.001$; inference: $r = 0.22$, $p = 0.006$, **Fig. 6e** & **Fig. 6f**, also see **Extended Data Fig. 8a**). Among the tracts between the EC and mPFC, the cingulum and uncinate show a significant correlation with inference performance, but not the fornix (**Extended Data Fig. 8b, c**).

Moreover, this EC-mPFC structural connectivity was closely linked to their functional interaction. This was evidenced by the correlation with the EC grid-modulated distance code from the mPFC in Game2 ($SC_{EC\text{-}mPFC}$: $r = 0.24$, $p = 0.003$, cingulum: $r = 0.23$, $p = 0.004$, **Fig. 6g**). This EC grid-modulated distance code was further found to mediate the effect of EC-mPFC structural connectivity on the inference performance in Game2 ($SC_{EC\text{-}mPFC}$: $\beta_{ab} = 0.07$, $p = 0.001$, CI [0.03, 0.13]). This is achieved, especially via the cingulum (cingulum: $\beta_{ab} = 0.07$, $p = 0.01$, CI [0.02, 0.13], **Fig. 6h**), rather than the uncinate or the fornix (all $p > 0.05$).

Together, these findings suggest that the maturation of the EC and mPFC, along with their structural connectivity, underpins the development of task representations and the associated flexible behaviour.

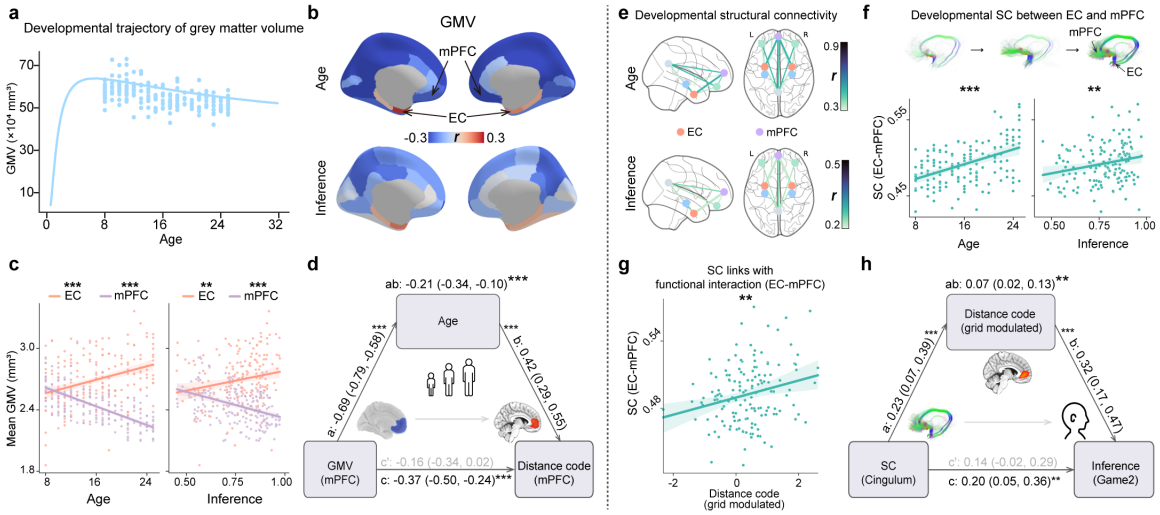

Fig. 6 | Structural basis of cognitive map through development. a, The developmental trajectory of grey matter volume (GMV) across the brain in relation to age, with data from the current study overlaid on the 'brain charts'[23]. Each dot represents an individual subject from the current study. It aligns well with the general decreasing pattern of grey matter volume from age 8 to 25 years. **b**, Regional correlations between cortical GMV and both age (top panel) and inference ability (bottom panel) for each of the 34 bilateral brain regions defined by the Desikan–Killiany parcellation[35]. Notably, the GMV in the EC increased with age and inference ability from ages 8 to 25, contrasting with the decreasing trend in most other regions. **c**, ROI analysis of the GMV in the bilateral EC and mPFC, highlighting the divergent developmental patterns in the EC (coral) and mPFC (purple). **d**, Mediation analysis indicated that age-related development mediated the influence of structural changes (GMV) in the mPFC on its task representation of the cognitive map (mean distance code across games). **e**, Developmental structural connectivity (SC). The SC was represented by the mean fractional anisotropy (FA) over white matter tracts connecting two brain areas, an index of tract coherence. The tract linking the EC and mPFC showed the highest correlation with age. The ROIs are EC (coral), mPFC (purple), HC (blue), LOFC (green), PCC (grey). **f,** Age-related increase in EC-mPFC structural connectivity, with tracts from representative subjects at age 8 (top left), 16 (top middle), 23 (top right). **g**, Positive correlation between EC-mPFC structural connectivity and the EC grid-modulated distance code in Game2. **h**, Mediation analysis indicated that the EC grid-modulated distance code mediates the impact of the EC-mPFC structural connectivity, particularly in the cingulum, on inference performance in Game2. Statistical inferences in mediation were derived using bootstrapping, with 10,000 iterations, and paths were labelled with coefficients and confidence intervals. Each dot represents data from an individual subject. **: $p < 0.01$, ***: $p < 0.001$.

Cognitive map-related measures generalize to established intelligence tests

Finally, we explored how the development of the cognitive map relates to specific cognitive abilities measured by standardized IQ tests. Rather than merely identifying correlations, we aimed to determine which aspects of intelligence, as assessed by IQ tests, closely align with the cognitive map-related measures during development.

We employed two well-known IQ tests: Raven's Standard Progressive Matrices (SPM) [37] and the Wechsler Intelligence Scale for Children (WISC) [38]. These tests evaluate a broad spectrum of cognitive abilities, ranging from working memory (like digit span tasks) to higher-level functions such as reasoning and comprehension of real-world concepts (e.g., 'explaining why seat belts are used in cars'). We found significant correlations between neural measures of the cognitive map—including task-related neural representations, brain structural development, and white matter connectivity—and various IQ scores (**Fig. 7a**).

To delve deeper into these relationships, we applied canonical correlation analysis (CCA), a statistical method that identifies the strongest associations between two sets of variables[39]. This analysis helped us uncover combinations of neural cognitive map measures and intelligence test scores that share the most variance (**Fig. 7b**). We utilized a strict permutation method, following the approach of Smith et al. [40] to minimize the possibility of false positives in the CCA. Only the first two canonical variates showed significant correlations (CV-1: $r = 0.64$, $p < 0.001$; CV-2: $r = 0.39$, $p = 0.009$; corrected for multiple comparisons; **Fig. 7c**).

The contributions of each neural measure of cognitive map to the different IQ domains are displayed in **Fig. 7d**. Notably, both the EC grid-like code and the mPFC distance code were significant predictors of SPM reasoning scores ($\beta_{\text{grid code}} = 0.55$, $p = 0.04$; $\beta_{\text{distance code}} = 0.52$, $p = 0.05$). To visualize these relationships, we projected the original measures onto the space defined by the first two canonical dimensions (**Fig. 7e**). This projection revealed that specific neural measures, such as the grid-like code and distance code, were closely associated with SPM reasoning scores and the WISC comprehension ability.

These particular IQ scores reflect children's abstract reasoning and understanding of relational concepts in the real world. This aligns with the roles of the grid-like and distance codes in representing the structured knowledge (schema and map) in our task.

Our findings suggest that the way children develop knowledge maps and utilise these maps to assimilate new information in the brain is connected to their ability to reason abstractly and comprehend complex concepts in everyday life.

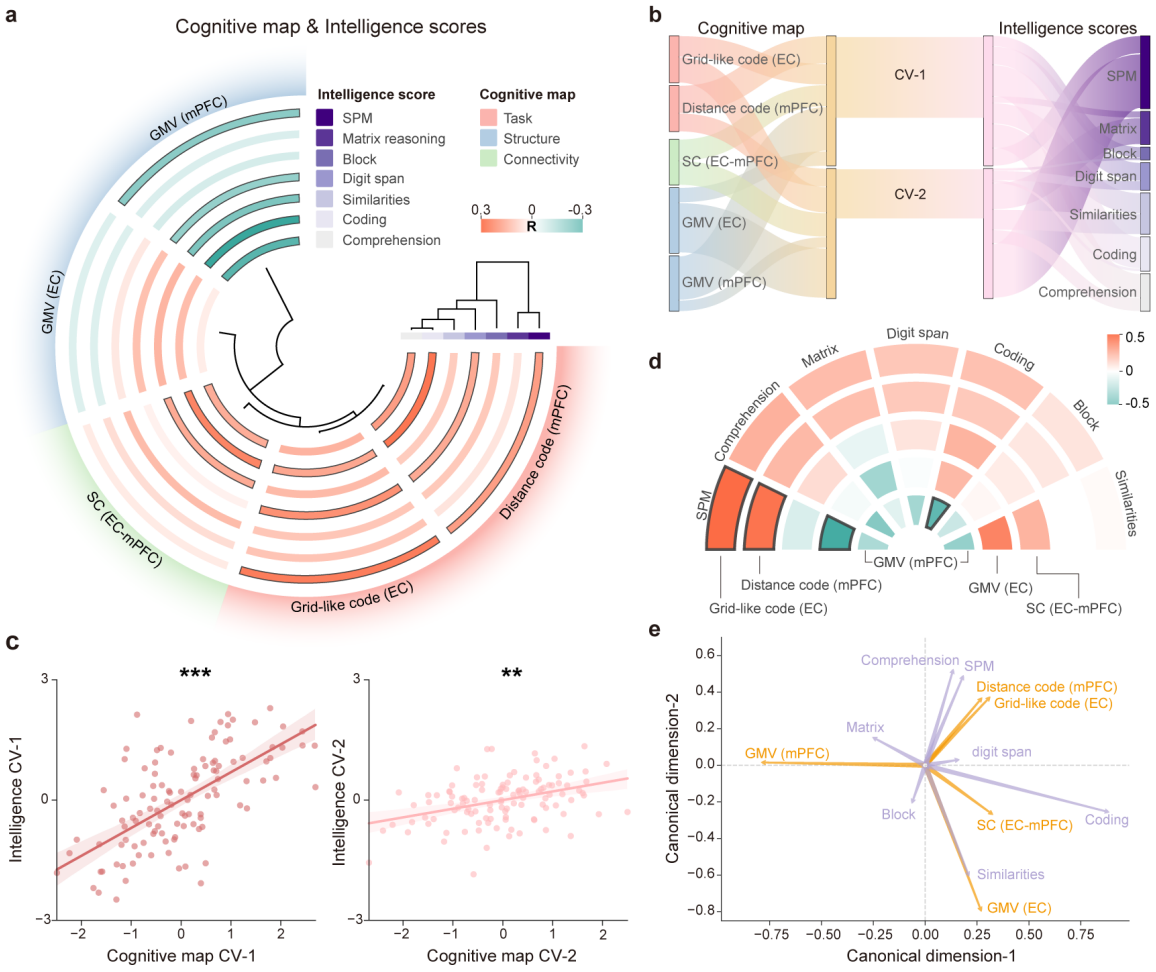

Fig. 7 | Neural signatures of cognitive map predict real-life intelligence scores. a, The heatmap illustrates the correlations between intelligence tests and neural signatures of cognitive map measures including task-related neural representations, structural development, and white matter connectivity. This heatmap is segmented into five sectors, each representing a different set of cognitive map measures, with rows in each sector detailing specific intelligence tests. The colour of each row indicates the strength and direction of correlation: blue for negative correlations and red for positive correlations. The hierarchical lines connecting elements in the circular diagram illustrate clustering patterns, indicating similarities within each category of measures. 'SPM' refers

to Raven's Standard Progressive Matrices, and other labels denote sub-tests within the WISC. **b**, The loading plot displays linear combinations of the original measures to the canonical correlation analysis (CCA) derived canonical variates. The width of each streamline indicates the contribution of each variable to the canonical variable and the correlations among the canonical variates. **c**, Scatter plots show the correlations between the first two canonical variates between neural cognitive map and intelligence measures. **d**, Coefficients of each neural signature from cognitive map for predicting intelligence domains using the CCA model. **e**, Projection of both sets onto the two-dimensional canonical space. Vectors, coloured purple for intelligence scores and orange for cognitive map measures, indicate the direction and magnitude of each measure within the canonical dimensions. The proximity and alignment of these vectors suggest a higher covariance among the measures. The black outlines indicate the statistically significant results in panels **a** and **d**. * $p < 0.05$, ** $p < 0.01$, *** $p < 0.001$.

Discussion

Our study explored how neural representations of structured knowledge emerge with age, leading to improved inferential reasoning abilities and real-world intelligence. We found that the maturation of grid-like neural codes—a fundamental cellular mechanism in the EC representing 2D knowledge maps—underpins the development of inferential reasoning and assimilation of new knowledge. These grid-like codes strengthen with age and support the mPFC in encoding distance relationships between concepts. The maturation of these neural codes also predicts real-world intelligence measures, particularly in children's abstract reasoning and understanding of relational concepts.

The grid-like code we identified resembles the firing patterns of grid cells initially discovered in animals, which are known to represent schemas of 2D physical spaces[15,17]. This schema representation captures the structural regularities in the environment, enabling generalization across different contexts. Previous fMRI studies have demonstrated similar grid-like mechanisms in humans in physical space[18] and, more recently, in abstract conceptual or social spaces[19,20]. Our results show that as individuals age, they exhibit increased proficiency in inferring unobserved relationships on a knowledge map. This improvement is mediated by a stronger grid-like code in the EC, suggesting that the organization of knowledge via schemas becomes more refined with development.

We also found that the consistency of the grid-like code in the EC between established and new maps facilitates the assimilation of new knowledge. This stable schema representation allows individuals to make novel inferences about new concepts more effectively, through mechanisms such as path integration[41,42]. Our findings align with animal studies showing that grid cells maintain consistent firing patterns across environments and adapt to incorporate new information, such as reward locations[43,44].

This highlights the broad applicability of the grid-like code in representing the general structural form of knowledge, resembling the concept of "core knowledge" in cognitive science[45]. It suggests that humans are born with innate abilities that provide basic intuitions about the world, forming the foundation for cognitive development[45]. Spatial understanding is a key example of this core knowledge[46]. For instance, young children around 3 or 4 years old primarily use specific objects as landmarks for orientation, whereas

adults can abstract spatial layouts to navigate[47]—paralleling the difference between map representations and schemas in our study.

Previous research suggested that young children have limited capacity for memory integration, particularly in tasks requiring associative inference[48,49]. However, our findings indicate that the development of structured knowledge organisation, which goes beyond simple enhancement in memory capacity. We controlled for memory differences, and the age-related improvements in inferential reasoning and assimilation abilities remained significant. Moreover, while memory reactivation can solve inference task, the map-based inference in our task benefits significantly from having an integrated 2D representation. For example, representing a 5×5 map requires remembering only 25 object-location relationships, as opposed to 400 pairwise associations needed if relying solely on memory integration. This abstraction of task structure from experiences involves efficient reorganization of memories, as also suggested by Roger Shepard[50,51,]. Such improvements cannot be explained by improvements in memory alone[52,53], nor can they explain the schema-related grid-like code in the EC.

A stable schema representation in the EC facilitates building new map representations by linking new information to existing knowledge. The mPFC plays a crucial role in this process[54]. We found that the mPFC encodes the distances between new and existing concepts on the knowledge map, and this distance code strengthens with age. Importantly, this effect remains significant even after controlling for memory performance and inferential reasoning abilities, indicating a unique, age-dependent development of mPFC representations in knowledge assimilation.

It should be noted that although we used Euclidean distance as the distance metric, very similar results were obtained when using Manhattan distance, which is unsurprising given the high correlation between the two in current design ($r = 0.93$). It is intriguing for future research to investigate what this distance code truly represents—whether it changes with alterations in environmental geometry, the presence of barriers, or extends beyond two dimensions. It would also be interesting to explore whether, in non-Euclidean environments, grid-like code continues to support the distance code and inferential reasoning or whether other alternative mechanisms come into play[55].

The mPFC continues to mature into adulthood, undergoing significant structural changes during adolescence[56-58]. These changes include alterations in grey matter volume and cortical thickness[56,59]. Our study observed distinct developmental trajectories in the EC and mPFC. While the mPFC grey matter volume decreases with age—consistent with known developmental patterns[23]—the EC grey matter volume increases, suggesting a prolonged maturation period. These structural changes support the functional representations of the cognitive map in both regions and contribute to the enhancement of inferential abilities.

Similarly, white matter connectivity in the brain develops steadily during adolescence, characterized by increasing axon density and myelination[60]. We observed significant age-related improvements in structural connectivity between the EC and mPFC, primarily through the cingulum bundle. The cingulum bundle constitutes the core of white matter in the cingulate gyrus[61], and serves as a crucial structural link in the default mode network involving the mPFC, and PCC, which are key areas associated with the grid code[19,20].

These structural and functional maturations coincide with the development of theory of mind (ToM)—the ability to infer others' thoughts and beliefs—which progresses with age and continues into late adolescence[62,63]. fMRI studies have shown that adolescents exhibit greater mPFC activity during mentalizing tasks compared to adults[64]. Our findings add a new dimension: the representational structure within the mPFC becomes more sophisticated with age. Given the critical role of the mPFC in both ToM and cognitive map, it is plausible that the development of mentalizing abilities and knowledge assimilation share common neural mechanisms.

These insights have important implications for education. Learning is fundamentally a process of knowledge assimilation, where new information is integrated into existing schemas[65]. In our study, the CCA revealed a close resemblance between neural measures of knowledge assimilation and advanced sections of IQ tests that assess reasoning and comprehension abilities during development. This finding suggests that educational strategies encouraging students to connect new concepts to their prior knowledge can enhance understanding[14,26,66]. Such schema-based learning approaches may be especially beneficial during adolescence, a critical period for neural development underlying the

cognitive map. This, in turn, may foster the development of reasoning and comprehension abilities that students can apply in real-world situation[67].

In conclusion, we demonstrate that the development of grid-like codes in the EC underpins inferential reasoning and assimilation. The mPFC supports this process by constructing new map representations based on schemas, a capability that matures with age. These functions are closely linked to the structural maturation of the EC and mPFC, as well as their connectivity. Together, our findings lay the groundwork for uncovering the cellular mechanisms that underpin the development of advanced human cognition.

Methods

Participants

We recruited a total of 231 subjects, with ages ranging from 8 to 25 years. Of these, 163 were between the ages of 8 and 18, ensuring a minimum of 10 subjects per age group. The remaining 68 were adults, aged 19 to 25, selected to reflect the later developmental stages of the mPFC as indicated by previous studies[23,24]. Subjects who were under 16 years old, were also scored on the Raven's Standard Progressive Matrices (SPM) test[37] and the Wechsler Intelligence Scale for Children (WISC) in accordance with the WISC grading norms for the Chinese population[38]. After excluding 28 participants (7 adults and 21 children) due to reasons such as failed memory training, excessive head movement during fMRI (with a mean FD exceeding 0.2 mm), and technical issues, we had a total of 203 participants (age: 15.64 ± 0.37, 115 female) for the primary analysis (**Extended Data Table 1**). Among them, 193 (age: 15.77 ± 0.39, 109 female) also undertook the subsequent knowledge assimilation phase after the primary inference task. In addition to the fMRI experiment, all participants underwent structural MRI scans, and 147 obtained diffusion MRI scans (age: 16 ± 0.43, 85 female). Before the actual experiment, those under 12 years old attended a mock scanner session. In this session, they watched a video introducing them to the sounds of magnetic resonance and highlighting the need to stay calm and motionless during the scan. This step helped younger participants practice head stability and become more comfortable with the MRI environment. All participants reported correct understanding of the task goal and instructions, both before and after the task.

The experiment protocol was approved by the Institutional Review Board of the Faculty of Psychology, Beijing Normal University (ethics number: IRB_A_0051_2021002). All participants were healthy with no history of psychiatric or neurological disorders, and provided informed consent before the task. For participants under 18 years old, parental consent was obtained. All procedures adhered to the standards set by the Institutional Review Board of Beijing Normal University.

Knowledge map

The knowledge map consists of a 5x5 grid spanning two independent dimensions: attack (AP) and defence power (DP), each with 5 rank levels. As in Park *et al.* [19], participants understood these ranks as equidistant intervals, enabling us to measure the hypothesized vector angle in the task space. The task space features 25 unique visual stimuli (monsters in the cover story). The association between a stimulus and its task space position is randomized for each participant, preventing any stimulus preference from skewing the task space representation on average.

During training, participants were not informed of the structure of the 2D knowledge map, such as the number of ranks per dimension, the count of stimuli sharing a rank, or their specific arrangement. Instead, they were given information specifically about the pairwise one-rank difference relationship within each dimension. In the formal fMRI task, our goal was to determine if and how participants, drawing from memory, constructed the knowledge map to enable flexible inference beyond just pairwise relationships.

Training procedure

Our training procedure was designed to ensure that all participants, regardless of age, memorised all pairwise relationships before proceeding to the formal fMRI experiment. This training was divided into three stages and could span multiple days if participants could not consistently meet the predefined standard. Participants learned 200 pairwise relationships during daily one-hour sessions (day: 12.79 ± 0.69).

Single Dimension Learning: In this initial stage, participants learnt the pairwise one-rank difference relationships for each dimension (DP and AP) separately. On any given day during this stage, they only learned pairs in one dimension, either AP or DP. The learning order between DP and AP was randomized across participants. During each trial, participants were presented with two stimuli differing by one rank within the specified dimension. A symbol at the screen's bottom indicated the dimension in focus, while a “>” or “<” sign in the centre denoted the rank relationship between the two stimuli (see **Fig. 1a**). Each of the 100 unique pairwise relationships within a dimension was shown twice,

with the positions of the stimuli swapped in the second presentation, resulting in 200 presentations per dimension.

To minimise the learning burden, the 200 pairs were split into 20 blocks. Participants learned each block repeatedly until they reached 80% accuracy. After completing this learning phase, participants underwent a probe test featuring all the pairs they had learnt. They had to achieve at least an 80% total accuracy rate to move on; otherwise, they repeated this stage.

Intermixed Learning: The second stage was similar to the first but with a key difference: trials for DP and AP dimensions were intermixed. Participants learned all 200 unique pairs (100 DP + 100 AP) with randomly swapped positions and sequences. This design aimed to prevent any order effect and to ensure participants retained the rank attributes of both AP and DP for each monster. Just like before, participants needed to achieve a minimum of 80% accuracy across both dimensions to advance. If they fell short, they repeated this stage.

Review: In the three days leading up to the formal fMRI experiment, participants reviewed all the pairs they had learnt, similar to the second stage. This final step ensured that every participant, regardless of age, entered the main task equipped with the necessary information to construct the mental map of the task. Consequently, if younger participants showed lower performance in cognitive map-based inference during formal fMRI experiment, it could not be attributed to information deficiencies.

Formal fMRI experiment

Subjects who had passed the training procedure were invited for the formal fMRI experiment. Upon arrival, they were probed again on their knowledge retention of all pairwise relationships. Probing trials for both dimensions were randomized, and no feedback was provided. The test performance served as an index for training accuracy (see **Fig. 1c**), the memory accuracy was 91.79 ± 0.34 %.

To ensure that all participants understood the task, each subject completed a pilot inference task. This pilot task had the same structure as the formal inference task but used different stimulus pairs (24 trials). This helped younger participants learn the rules and become

familiar with the task. After completing the pilot task, participants were asked to report the task rules to confirm their understanding.

Subjects then participated in a 2D inference task while undergoing concurrent fMRI scanning. Unlike traditional transitive inference tasks, this required integrating information from both dimensions. Participants had to determine if the AP order of one monster was higher than the DP order of another. The decision rule, which identified the attacker and defender, varied trial by trial and was only revealed after the presentation of the second monster (M2). This design encouraged subjects to maintain a 2D knowledge map in mind during M2 presentation, and only compute value upon the decision rule. This was shown to be effective (see **Extended Data Fig. 3**).

Following this, subjects were invited to engage in a novel knowledge assimilation task. In this phase, four new objects were introduced to the map for the first time. After learning their relationships with nearby monsters on the map (local learning), subjects were tasked to infer the relationships between these new entities and non-adjacent ones, with which they had no direct learning experience (non-local inference), all while undergoing fMRI scanning.

2D inference task

During the fMRI scanning, the main task involved participants inferring relationships between two monsters based on their ranks in both AP and DP dimensions, termed "2D inference". Each trial began with a 0.5s fixation, followed by the appearance of the first monster (M1) for 1-4s. The second monster (M2) then appeared for 2.5s, followed by a jittered inter-stimulus-interval (ISI) of 1-4s. Upon the appearance of M2, participants could mentally navigate the 2D knowledge map by drawing a hypothesized vector that connected M1 and M2. Subsequently, the decision rule, accompanied by the target dimension symbols for both monsters, was presented for up to 3s and disappeared upon choice. Each trial ended with an inter-trial-interval (ITI) that lasted between 0.3-3.3s. The main task consisted of 252 trials, divided into 6 runs, covering all possible angles on the 5x5 map with 21 trials for each angle bin (12 bins in total, equally spanned 0-2π). The presentation order of monsters within-pair were randomized.

Knowledge assimilation task

To investigate how the cognitive map was utilized for assimilating new knowledge, subjects subsequently participated in a novel knowledge assimilation task. Four new monsters, each represented by a unique visual stimulus, were introduced around the centre of the existing map.

During this phase, participants learnt the relative rank differences of these new monsters with the adjacent existing ones, a process termed "local learning". They acquired these new pairwise relationships using the same procedure as in the previous learning phase. Participants were informed that the relationships between existing objects would remain unchanged, allowing them to assimilate the new knowledge into a consistent framework.

This learning phase consisted of 256 trials, split evenly with 128 trials for each dimension. Each local-pair relationship was presented 8 times. After learning, participants underwent a probe test encompassing all the learned pairs. The mean accuracy achieved was 83.32 ± 1.01 %.

Following this, subjects engaged in a 2D inference task, which was structured identically to the main task in terms of timing and trial structure. However, this task exclusively focused on the relationships between the new monsters and the non-local ones, which were not included in the learning set. This non-local inference was conducted concurrently with fMRI scanning. Overall, 84 unique pairs were presented, with each new monster being paired with 21 non-local existing monsters. Trials were randomized and evenly split across 2 runs.

Behavioural analysis

We evaluated age-related behavioural improvements in map-based inference (Game1) and nonlocal inference (Game2) using Pearson correlation and its partial correlation variant. For Game1, the partial correlation analysis included training accuracy as a covariate to control for memory performance, which also tend to improve with age. To assess the selective developmental impact on knowledge assimilation in Game2, we conducted a partial correlation, adjusting for Game1 performance and the learning performance of

newly introduced objects. Additionally, linear regression models were performed to support the findings both in Game1 and Game2. In Game1, the model including age and memory performance, showed a significant age effect on map-based inference performance. In Game2, the regression model included age, Game1 performance, and memory performance during training and new knowledge learning as explanatory variables, with nonlocal inference as the dependent variable.

MRI data acquisition

We acquired structural image and functional images on Siemens Prisma 3T scanner. T2-weighted functional images were acquired using an echo planar imaging (EPI) sequence with the following parameters: 49 slices in an interleaved order repetition time, resolution = 3 × 3 × 3 mm^3, repetition time (TR) = 3000 ms, echo time (TE) = 30 ms, flip angle = 90°, field of view (FoV) = 192 mm. We used a 30° slice angle relative to the anterior-posterior commissure line to minimize signal loss in the orbitofrontal cortex region [68]. We also acquired a T1-weighted structural image using a magnetization-prepared rapid gradient echo (MPRAGE) sequence with the following parameters: resolution = 0.5 × 0.5 × 1 mm^3, TR = 2530 ms, TE = 2.98 ms, flip angle = 7°, FoV = 256 mm. The diffusion data were acquired using a spin-echo diffusion-weighted sequence with the following parameters: resolution = 2 × 2 × 2 mm^3, 64 diffusion direction, TR = 2800 ms, TE = 75 ms, b = 0, 1000, 2000, 3000 s/mm^2, PA phase encode direction. Phase-reversed b0 images were collected to derive a fieldmap for distortion correction of diffusion data.

MRI Data preprocessing

Results included in this manuscript come from preprocessing performed using fMRIPrep 20.2.7[69] and QSIPrep 0.19.0, which are based on Nipype[70].

Structural data preprocessing

The T1-weighted (T1w) image was corrected for intensity non-uniformity (INU) with N4BiasFieldCorrection[71], distributed with ANTs 2.3.3[72], and used as T1w-reference throughout the workflow. The T1w-reference was then skull-stripped with a Nipype implementation of the antsBrainExtraction.sh workflow (from ANTs), using

OASIS30ANTs as target template. Brain tissue segmentation of cerebrospinal fluid (CSF), white-matter (WM) and grey-matter (GM) was performed on the brain-extracted T1w using fast[73]. Volume-based spatial normalization to one 2 mm standard space (MNI152NLin2009cAsym) was performed through nonlinear registration with antsRegistration (ANTs 2.3.3), using brain-extracted versions of both T1w reference and the T1w template. The following template was selected for spatial normalization: ICBM 152 Nonlinear Asymmetrical template version 2009c MNI152NLin2009cAsym[74].

Functional data preprocessing

For each run, the following preprocessing was performed. First, a reference volume and its skull-stripped version were generated using fMRIPrep. A deformation field to correct for susceptibility distortions was estimated based on fMRIPrep's fieldmap-less approach. The deformation field is that resulting from co-registering the BOLD reference to the same-subject T1w-reference with its intensity inverted[75,76]. Registration is performed with antsRegistration (ANTs 2.3.3), and the process regularized by constraining deformation to be nonzero only along the phase-encoding direction, and modulated with an average fieldmap template[77]. Based on the estimated susceptibility distortion, a corrected EPI (echo-planar imaging) reference was calculated for a more accurate co-registration with the anatomical reference.

The BOLD reference was then co-registered to the T1w reference using flirt[78] with the boundary-based registration[79] cost-function. Co-registration was configured with nine degrees of freedom to account for distortions remaining in the BOLD reference. Head-motion parameters with respect to the BOLD reference (transformation matrices, and six corresponding rotation and translation parameters) are estimated before any spatiotemporal filtering using mcflirt[80].

BOLD runs were slice-time corrected to 1.46s (0.5 of slice acquisition range 0s-2.92s) using 3dTshift from AFNI 20160207[81]. The BOLD time-series (including slice-timing correction when applied) were resampled onto their original, native space by applying a single, composite transform to correct for head-motion and susceptibility distortions. These resampled BOLD time-series will be referred to as preprocessed BOLD in original space,

or just preprocessed BOLD. The BOLD time-series were resampled into standard space, generating a preprocessed BOLD run in MNI152NLin2009cAsym space.

Several confounding time-series were calculated based on the preprocessed BOLD: FD and three region-wise global signals. For each run, FD with root mean square matrix were calculated following the definitions by Jenkinson *et al.* [80]. The three global signals are extracted within the CSF, the WM, and the whole-brain masks. The head-motion estimates calculated in the correction step were also placed within the corresponding confounds file. Frames that exceeded a threshold of 0.5 mm FD were annotated as motion outliers.

All resamplings can be performed with a single interpolation step by composing all the pertinent transformations (i.e., head-motion transform matrices, susceptibility distortion correction when available, and co-registrations to anatomical and output spaces). Gridded (volumetric) resamplings were performed using antsApplyTransforms (ANTs), configured with Lanczos interpolation to minimize the smoothing effects of other kernels[82]. Non-gridded (surface) resamplings were performed using mri_vol2surf (FreeSurfer).

Diffusion data preprocessing

Preprocessing of the diffusion data was conducted using QSIPrep 0.19.0, built on Nipype 1.8.6[70,83]. In this process, images with a b-value less than 100 s/mm^2 were classified as b=0 images. We applied MP-PCA denoising, using MRtrix3's dwidenoise tool with a 5-voxel window, following the method outlined by Veraart et al. [84]. Post-denoising, we adjusted the mean intensity of the DWI series so that the mean intensity of b=0 images was matched across different DWI scans. Correction for B1 field inhomogeneity was done using MRtrix3's dwibiascorrect with the N4 algorithm[71].

For head motion and Eddy current correction, we employed FSL's eddy tool, following the guidelines of Andersson and Sotiropoulos [85]. Our configuration for eddy included a q-space smoothing factor of 10, five iterations, and the use of 1000 voxels for estimating hyperparameters. We applied linear models at both first and second levels to account for Eddy current-related spatial distortion. Shells were assigned to q-space coordinates, and an effort was made to separate field offset from subject movement. Eddy's outlier replacement

was run following Andersson et al. [86]. We grouped the data by slice and any group deviating more than four standard deviations from the prediction had their data replaced with imputed values.

Data collection involved the use of reversed phase-encode blips to generate image pairs with opposite directional distortions. For this, we used b=0 reference images with reversed phase encoding and an equal number of b=0 images from the DWI scans. The susceptibility-induced off-resonance field was estimated from these pairs, following[87]. The resulting fieldmaps were then incorporated into the interpolation process for Eddy current and head motion correction, with the final interpolation being performed using the 'jac' method.

In the final stage of preprocessing, we calculated several confounding time-series based on the preprocessed DWI, including FD. Finally, the DWI time-series were resampled to ACPC, resulting in a preprocessed DWI ru n in ACPC space with 2 mm isotropic voxels.

Functional MRI data analysis

We performed general linear model (GLM) to capture event-related activations. The preprocessed data were smoothed with an 8-mm full-width at half maximum Gaussian kernel and filtered by a high-pass cutoff filter of 100 Hz. All GLMs modelled three basic events (M1, M2, Decision) as regressors. This was achieved by using a boxcar function with the corresponding duration, which accounted for the mean response specific to those visual stimuli that were not of interest (see **Extended Data Fig. 4** for related activation patterns). All regressors were convolved with a canonical hemodynamic response function. In an effort to mitigate the effects of potential head motion noise, all GLMs incorporated six rigid-body motion parameters (3 translation and 3 rotation parameters), in addition to the motion outliers, cerebrospinal fluid (CSF) and white matter (WM) signals in each run.

We modelled parametric regressors for different target representations: grid-like code, distance code, and value code, as described below. Further second-level covariate analysis were performed with one-sample t-test using age or inference performance as the covariate.

Grid-like code

To detect grid-like code in fMRI, we used three established and independent methods: first, a hexagonal modulation analysis that relies on the *z*-transformed *F*-statistic of inferred trajectories[20,27]; second, an analysis of the hexagonal consistency effect, which compares inferred trajectories with the mean orientation of a specific brain region, such as the EC[18,19]; and third, a similarity analysis focused on the neural representations of angular differences in inferred trajectories[28].

In the hexagonal modulation analysis, we began by determining the angle, θ, of the inferred trajectory. This process starts with the presentation of M2, from which a trajectory on the 2D map can be inferred. Consequently, the GLM modelled a six-fold sinusoidal modulation with two parametric regressors: sin6θ and cos6θ at the time of M2's presentation and decision. Here, θ represents the direction of inferred trajectories in each trial. We modelled the events for correct trials and error trials separately, setting those parametric modulations on correct trial events. The parametric estimates of these two regressors form a quadrature filter, with its amplitude ($\sqrt{\beta_{sin}^2 + \beta_{cos}^2}$) being sensitive to hexagonal symmetry. To compute this amplitude, we applied an *F*-test to detect any linear combination of these two regressors: $\beta_{sin} * \sin(6\theta) + \beta_{cos} * \cos(6\theta)$ [18,20]. Then, we transformed the statistic at the first level into *z*-statistic based on an asymptotic approximation for further group-level analysis[88]. This analysis was conducted for both Game1 and Game2. Similar to previous studies[20], the *F*-test-based method didn't account for consistent mean orientation across runs. It allowed us to define a functional EC ROI in an unbiased manner. This mask was just used to estimate mean orientation and included voxels with hexagonal symmetry at a threshold of $p = 0.001$ in the anatomical EC mask.

In the analysis of the hexagonal consistency effect, we employed a cross-validation procedure. We first estimated the mean orientation of the grid signal using one half of the dataset and then tested the hexagonal consistency on the remaining half. In training GLM, we modelled two 6-fold sinusoidal parametric regressors (sin(6θ) & cos(6θ)) separately for odd and even trials at the time of M2's presentation and decision. We estimated the mean orientation φ for each participant within the *F*-test-based EC ROI, separately for both odd

and even trials. The orientation φ of each voxel in the EC was calculated from the β coefficient of the sine and cosine regressors using the formula: $\varphi = \frac{\arctan\left(\frac{\beta_{sin}}{\beta_{cos}}\right)}{6}$. We calculated the mean orientation for each subject by averaging the estimated orientation across voxels in the EC ROI using the circular mean. Next, we incorporated the mean orientation into a test GLM to estimate the hexagonal consistency effect aligned with the mean orientation. The test GLM maintained the regressors of basic events and nuisance regressors but modelled the sinusoidal modulation with the regressor: $\cos(6[\theta - \varphi])$ instead of previous parametric modulations (sine & cosine) for odd and even trials. Here, θ refers to the direction of inferred trajectories in each trial, and φ represents the estimated mean orientation for each participant. Importantly, we applied the mean orientation estimated from the odd trials of training GLM to the even trials of the test GLM, and vice versa. This cross-validation procedure was also repeated for other periodicities, including 4-fold, 5-fold, 7-fold and 8-fold. Based on this cross-validation procedure, we categorized the inferred directions into 12 equal bins based on whether the directions aligned or misaligned with the estimated mean orientation. We modelled regressors for each bin to estimate their mean activities at the time of M2's presentation to unfold the pattern of hexagonal activity.

The grid-like code can also be measured based on RSA[89]. The first step of this analysis involved the construction of a model for the representational dissimilarity matrix (RDM) to depict grid-like representation, as detailed in Bellmund *et al.* [28]. The model RDM hypothesized that the similarity of neural activity is contingent upon the angular difference between inferred directions, an attribute stemming from the 6-fold periodicity of grid-like activity. The activity patterns showed a greater degree of similarity for angular differences within the 0-15° and 45-60° range, as opposed to the intermediate angular range of 15-45°. This pattern exhibits a cyclical nature, spanning from 0° to 360° with a recurring period of 60°. Consequently, the similarity in activity between any two directions can be divided into two distinct categories: similarity and dissimilarity. This classification enabled us to construct a model RDM for the grid representation, predicated on the similarity between pairs of inferred directions. In this RDM, we assigned a value of zero to similarity and one to dissimilarity.

Subsequently, we conducted a whole-brain searchlight analysis to compute the neural RDM of the inferred directions for each voxel. For this purpose, we modelled an independent regressor for each direction at the time of M2's presentation in the GLM to estimate the mean activities of each inferred direction. Following this, for each voxel, we obtained its searchlight sphere that included its surrounding multi-voxels. The neural RDM of each sphere was estimated by calculating the correlation distance $(1 - r)$ between the multivariate activity patterns associated with different directions. We then evaluated the representation similarity between the grid model RDM and the neural RDM, using Pearson's correlation. The resulting correlation coefficients were re-mapped to the central voxel associated with each sphere and were subsequently transformed into z-scores for each brain voxel.

In Game2, we conducted a GLM to estimate a map alignment effect between two maps. The map alignment effect was quantified by the amplitude of hexagonal modulation in the knowledge-assimilated map aligned with the grid angle of the original map. Specifically, we used a similar cross-validation procedure as above to estimate the mean orientation φ_{game1} from the β coefficients of two 6-fold sinusoidal parametric regressors ($\sin(6\theta)$ & $\sin(6\theta)$) from Game1's data. We then incorporated this mean orientation into a sinusoidal parametric regressors ($\cos\left(6\left[\theta_{game2} - \varphi_{game1}\right]\right)$ in test GLM on the Game2's data. Here, the θ_{game2} refers to the direction of inferred trajectories in Game2, which traverse pre-existing objects and new objects. The positions of new objects were hypothesized around the centre of the map and had a half-rank distance with pre-existing objects.

Distance code

We adopted fMRI adaptation to measure the neural representation similarity between objects when inferring the relationship for novel pairs during mental navigation. This method evaluates neural representation similarity by measuring suppression or enhancement when two stimuli are presented in rapid succession[90]. We modelled the Euclidean distance between objects as parametric regressor during the presentation of M2. This Euclidean distance was calculated by the square root of the sum of the squared differences between their AP dimension and DP dimension, as following formula: $d_{2D} =$

$\sqrt{(AP_{M2} - AP_{M1})^2 + (DP_{M2} - DP_{M1})^2}$. We also modelled the 1D rank difference in the AP and DP dimensions as parametric regressors in the GLMs for comparison with the 2D Euclidean distance representations.

Value code

We modelled value code as a parametric modulation during the presentation time of the fight rule. During this time, subjects were required to make a decision by comparing the Attack Power (AP) of the attacking monster with the Defence Power (DP) of the defending monster to calculate the decision variables. In our first level of analysis, we modelled two potential decision variables: the absolute value of difference $|AP - DP|$ and the difference of value $(AP - DP)$. We also performed a GLM which included both the distance code and value code at the presentation time of M2 and decision. In this GLM, the distance code was modelled using Euclidean distance and the value code at decision-making was modelled using absolute value of difference $|AP - DP|$. The value code at the presentation time of M2 was defined by the mean of two possible decision values $|AP_{M1} - DP_{M2}|$ and $|AP_{M2} - DP_{M1}|$, due to the rule being unknown at this stage.

Conjunction analysis

After identifying the cognitive map representations in both games, we conducted a conjunction analysis to compare the representations of the original and knowledge-assimilated maps. This comparison was made for both the grid-like code and distance code at whole-brain level. We computed the area of overlap across the significant statistical maps of both Game1 and Game2 for grid-like code and distance code. It is important to note that all group maps that were included in the conjunction analysis had already been corrected for multiple comparisons to ensure the statistical significance of the areas of conjunction.

Structural MRI data analysis

We reconstructed the cortical surfaces from T1-weighted MRI scans using FreeSurfer and obtained measurements of grey matter volume and thickness from individual surfaces[33,34].

The characteristics of the grey matter were then segmented into the 34 bilateral brain regions defined by the Desikan–Killiany parcellation[35]. For each brain region, we computed the Pearson correlation between its grey matter characteristics and both age and inference ability. Subsequently, these results were projected onto the corresponding surface parcellation. These correlation results were then projected onto the corresponding surface parcellation. We analysed the hippocampal volume derived from FreeSurfer's brain segmentation using a similar procedure.

Structural connectivity analysis

Fiber reconstruction was conducted using QSIprep 0.19.0, based on Nipype 1.8.6[70,83]. To achieve more accurate tissue boundary delineation, we employed a hybrid surface/volume segmentation approach, as proposed by Smith et al. [91]. The outputs from FreeSurfer, along with previously defined ROIs, specifically, EC, mPFC, PCC, LOFC, and hippocampus, were registered to the outputs preprocessed by QSIPrep.

For the estimation of multi-tissue fiber response functions, we utilized the algorithm from Dhollander et al. [92]. Fiber orientation distributions (FODs) in each voxel were then estimated using constrained spherical deconvolution (CSD), following the methodologies of [93,94], and employing an unsupervised multi-tissue method as described by Dhollander et al. [95]. The FODs underwent intensity normalization using mtnormalize[96].

The actual fiber reconstruction was executed in MRtrix3[96,97]. This process incorporated anatomically constrained tractography[98] and spherical-deconvolution informed filtering of tracts[99], thereby enhancing the biological plausibility and accuracy of the fiber connectivity measures.

To further analyze structural connectivity, we extracted and averaged FA values for the reconstructed tracts connecting pairs of ROIs. Initially, we fitted the diffusion tensor to the preprocessed diffusion-weighted images using iterated weighted least squares (IWLS) via MRtrix3. This process enabled the computation of fractional anisotropy (FA) across the brain[36,100]. Subsequently, the FA values were sampled from the FA image and averaged for each streamline. Then, for each connectome edge, the mean value was calculated by

averaging the FA of all streamlines connecting the target pair, indexing the structural connectivity between ROIs.

To conduct a more detailed analysis of tracts connecting the EC and mPFC, we utilized labeled white-matter tracts from an independent atlas to identify the three canonical tracts: the cingulum bundle, uncinate fasciculus, and fornix[101]. These white-matter tracts connect the frontal lobe and temporal lobe via distinct pathways. In this analysis, we mapped streamlines from this atlas into probability density maps using MRtrix3. We applied a 10% threshold to these maps, creating three binary masks. These masks were then transformed to individual spaces, aligning with the FA images. Finally, we used these three masks to extract the mean FA values of the white-matter tracts.

ROI analysis

We also examined the grid-like code, distance code, value code and structural measurements, as well as their relationships with age and inference performance at ROI level. We employed five ROIs that were independently defined outside of our study, including the EC, mPFC, hippocampus, LOFC and PCC. We used a bilaterally, anatomically defined EC ROI based on the Juelich Histological Atlas[29]. The hippocampus ROI was defined based on Harvard-Oxford subcortical structural atlas[35]. The mPFC ROI was defined based on a vmPFC mask from NeuroVault (https://identifiers.org/neurovault.image:18650). The LOFC ROI was defined based on the Desikan–Killiany parcellation[35]. The PCC ROI was defined based on the parcellation of default mode network from NeuroVault (https://identifiers.org/neurovault.image:319482) [102].

In functional analysis, we averaged the parameter estimates or z-scores obtained from the first level analysis or RSA across all voxels within each ROI. We performed one sample t-tests to determine the significance of mean effect within each ROI. In correlation analysis, we standardized these values obtained from the first level analysis across subjects and examined their correlation with age and inference performance. We utilized a paired t-test to compare various scenarios: alignment versus misalignment, 2D distance versus 1D distance, and "$abs(AP - DP)$" versus "$AP - DP$". We also performed an analysis of

variance to investigate whether a significant interaction effect exists between task stage (mental navigation and decision-making) and representational content (distance code and value code).

In structural analysis, the identical ROIs, defined in the same manner as in the fMRI analysis, were registered to the FreeSurfer's fsaverage template. The individual grey matter volume and thickness were also mapped onto the fsaverage template. We extracted the corresponding grey matter characteristics from the ROIs. Then we calculated their correlations with age, inference performance, and the strength of task representations.

Mediation analysis

We execute mediation analysis with a non-parametric bootstrap method[32,103] to investigates how the influence of an independent variable X on a dependent variable Y is partially mediated by a third variable M. We derived statistical inference with a total of 10,000 iterations to generate confidence intervals (CI) and the two-sided p-value of indirect effect. The coefficients and confidence intervals of indirect effect were reported in Results.

We performed a series of path models to probe whether the task representations mediate the impact of development on inference performance. In these models, age was positioned as the independent variable (X), and inference performance served as the dependent variable (Y). We used the grid-like code within the EC, as well as the distance code and value code within the mPFC, as mediators. Prior to conducting the mediation, all metrics were standardized across subjects. For representations that showed significant indirect effects (grid-like code & distance code), we also performed a parallel mediation analysis that included both mediators. To test the relationship between grid-like code, distance code and inference performance, we performed a mediation analysis among the distance code within mPFC (X), grid-like code within EC (M), and map-based inference performance (Y). In the analysis of Game2, the map-based inference performance (Game1) was additionally incorporated into the paths of mediation analysis as covariate. Finally, we conducted mediation analyses by including age as a mediator, the structural features (grey matter volume & grey matter thickness) as an independent variable (X), and the task representations as the dependent variable (Y).

Canonical correlation analysis (CCA)

We performed CCA to explore the relationship between cognitive map measures and intelligence scores. This analysis involved identifying a set of canonical variates—linear combinations of the original variables designed to maximize correlations between two sets of variables. To compute these canonical components, we employed the nonlinear iterative partial least squares (NIPALS) algorithm[39]. This algorithm iteratively ensures the orthogonality of successive variates by removing the variance of each identified component from the original data. After generating a series of weights for these linear combinations, we applied them to compute the canonical variates. We then calculated the loadings by correlating the canonical variates with the original measures, thereby illustrating the association between the original measures and the canonical variates. Finally, to determine the canonical correlation, we computed Pearson's correlation between the canonical variates derived from cognitive map measures and intelligence scores. Statistical significance was assessed using 10,000 permutations, which involved randomizing the order of subjects within each measure set[40]. For each permutation, we reran the CCA to establish a valid null distribution, against which we compared the actual correlations. *P*-values were corrected for multiple comparisons across all modes estimated. The significance of each predictive coefficient was similarly estimated using this permutation approach.

Statistical analysis

We presented the mean and standard error throughout both the figures and the manuscript. Statistical significance was reported using two-tailed *p*-values, except for the comparison between the alignment and misalignment conditions, where we used a one-tailed paired t-test based on our hypothesis that alignment would be greater. For one-sample *t*-tests, Cohen's *d* effect sizes were calculated by dividing the mean of each group by its standard deviation. For paired *t*-tests, Cohen's *d* was determined by dividing the mean difference between groups by the pooled standard deviation of both samples.

In the fMRI analysis, multiple comparison corrections were performed using the FMRIB Software Library (FSL) software[104]. Significant brain regions were reported with whole-

brain family-wise error (FWE) correction at the cluster level ($p < 0.05$), with a cluster-forming voxel threshold of $p < 0.001$, except for the EC. Due to susceptibility to signal loss in the EC, a more lenient cluster-forming voxel threshold of $p < 0.01$ was used, as commonly reported in previous studies [19,20].

For the ROI analyses, we focused on predefined regions based on prior hypotheses: the grid-like code in the EC and the distance code in the mPFC. No statistical inferences were made beyond these specific ROIs, as our analyses were hypothesis-driven and limited to these regions, reducing the risk of multiple comparison issues.

We also conducted multiple correlations between measures of intelligence from standardised IQ tests and cognitive map-based inference from our study. To control for false positives, we used permutation tests within a CCA framework. This non-parametric approach, following Smith *et al.* [40], effectively adjusted for multiple comparisons, enhancing the reliability of our findings.

All analyses were conducted using Python and its libraries, including Nilearn, statsmodels, Pingouin, scikit-learn, and rsatoolbox, along with the FSL. The circular heatmap was generated using ChiPlot (https://www.chiplot.online).

Acknowledgment

Conceptualization, Y.L., Y.Q., and T.B.; Investigation, Q.Y., J.O., L.P., S.W., Y.Luo., Y.L., and T.B.; Writing – Original Draft, Y.Q., Y.L.; Writing – Review & Editing, Y.Q., Y.L., J.O., and T.B. This study is supported by the National Science and Technology Innovation 2030 Major Program (2022ZD0205500), the National Natural Science Foundation of China (32271093), the Beijing Natural Science Foundation (Z230010, L222033), and the Fundamental Research Funds for the Central Universities.

Conflict of interest

The authors have indicated they have no potential conflicts of interest to disclose.

Data availability

fMRI and behavioural data that support the conclusions in this study will be available on https://osf.io/ajz6g/ upon publication. The raw individual participant MRI data will be available upon reasonable request to the corresponding author, subject to participant consent.

Code availability

The analysis code will be publicly available on https://gitlab.com/liu_lab/develop_cognitive_map.git upon publication.

References

1. Tolman, E.C. (1948). Cognitive maps in rats and men. Psychological review *55*, 189.
2. Piaget, J., and Cook, M. (1952). The origins of intelligence in children (International Universities Press New York).
3. Piaget, J. (1926). The language and thought of the child.
4. Piaget, J. (1972). Intellectual evolution from adolescence to adulthood. Human development *15*, 1-12.
5. Andrews, G., and Halford, G.S. (1998). Children's ability to make transitive inferences: The importance of premise integration and structural complexity. Cognitive Development *13*, 479-513.
6. Schlichting, M.L., Guarino, K.F., Schapiro, A.C., Turk-Browne, N.B., and Preston, A.R. (2017). Hippocampal structure predicts statistical learning and associative inference abilities during development. Journal of cognitive neuroscience *29*, 37-51.
7. Pudhiyidath, A., Roome, H.E., Coughlin, C., Nguyen, K.V., and Preston, A.R. (2020). Developmental differences in temporal schema acquisition impact reasoning decisions. Cognitive Neuropsychology *37*, 25-45.
8. Behrens, T.E., Muller, T.H., Whittington, J.C., Mark, S., Baram, A.B., Stachenfeld, K.L., and Kurth-Nelson, Z. (2018). What is a cognitive map? Organizing knowledge for flexible behavior. Neuron *100*, 490-509.
9. Whittington, J.C., McCaffary, D., Bakermans, J.J., and Behrens, T.E. (2022). How to build a cognitive map. Nature neuroscience *25*, 1257-1272.
10. Stachenfeld, K.L., Botvinick, M.M., and Gershman, S.J. (2017). The hippocampus as a predictive map. Nature neuroscience *20*, 1643-1653.
11. Dayan, P. (1993). Improving generalization for temporal difference learning: The successor representation. Neural computation *5*, 613-624.
12. Mark, S., Moran, R., Parr, T., Kennerley, S.W., and Behrens, T.E. (2020). Transferring structural knowledge across cognitive maps in humans and models. Nature communications *11*, 4783.
13. Halford, G.S., Bain, J.D., Maybery, M.T., and Andrews, G. (1998). Induction of relational schemas: Common processes in reasoning and complex learning. Cognitive psychology *35*, 201-245.
14. Bartlett, F.C. (1995). Remembering: A study in experimental and social psychology (Cambridge university press).
15. Hafting, T., Fyhn, M., Molden, S., Moser, M.-B., and Moser, E.I. (2005). Microstructure of a spatial map in the entorhinal cortex. Nature *436*, 801-806.
16. Jacobs, J., Weidemann, C.T., Miller, J.F., Solway, A., Burke, J.F., Wei, X.-X., Suthana, N., Sperling, M.R., Sharan, A.D., and Fried, I. (2013). Direct recordings of grid-like neuronal activity in human spatial navigation. Nature neuroscience *16*, 1188-1190.
17. Fyhn, M., Hafting, T., Treves, A., Moser, M.-B., and Moser, E.I. (2007). Hippocampal remapping and grid realignment in entorhinal cortex. Nature *446*, 190-194.
18. Doeller, C.F., Barry, C., and Burgess, N. (2010). Evidence for grid cells in a human memory network. Nature *463*, 657-661.
19. Park, S.A., Miller, D.S., and Boorman, E.D. (2021). Inferences on a multidimensional social hierarchy use a grid-like code. Nature neuroscience *24*, 1292-1301.

20. Constantinescu, A.O., O'Reilly, J.X., and Behrens, T.E. (2016). Organizing conceptual knowledge in humans with a gridlike code. Science *352*, 1464-1468.
21. Piaget, J. (2005). The psychology of intelligence (Routledge).
22. Tse, D., Takeuchi, T., Kakeyama, M., Kajii, Y., Okuno, H., Tohyama, C., Bito, H., and Morris, R.G. (2011). Schema-dependent gene activation and memory encoding in neocortex. Science *333*, 891-895.
23. Bethlehem, R.A., Seidlitz, J., White, S.R., Vogel, J.W., Anderson, K.M., Adamson, C., Adler, S., Alexopoulos, G.S., Anagnostou, E., and Areces-Gonzalez, A. (2022). Brain charts for the human lifespan. Nature *604*, 525-533.
24. Casey, B., Giedd, J.N., and Thomas, K.M. (2000). Structural and functional brain development and its relation to cognitive development. Biological psychology *54*, 241-257.
25. Bauer, P.J., Dugan, J.A., Varga, N.L., and Riggins, T. (2019). Relations between neural structures and children's self-derivation of new knowledge through memory integration. Developmental cognitive neuroscience *36*, 100611.
26. Bauer, P.J. (2021). We know more than we ever learned: Processes involved in accumulation of world knowledge. Child development perspectives *15*, 220-227.
27. Bongioanni, A., Folloni, D., Verhagen, L., Sallet, J., Klein-Flügge, M.C., and Rushworth, M.F. (2021). Activation and disruption of a neural mechanism for novel choice in monkeys. Nature *591*, 270-274.
28. Bellmund, J.L., Deuker, L., Navarro Schröder, T., and Doeller, C.F. (2016). Grid-cell representations in mental simulation. Elife *5*, e17089.
29. Amunts, K., Kedo, O., Kindler, M., Pieperhoff, P., Mohlberg, H., Shah, N., Habel, U., Schneider, F., and Zilles, K. (2005). Cytoarchitectonic mapping of the human amygdala, hippocampal region and entorhinal cortex: intersubject variability and probability maps. Anatomy and embryology *210*, 343-352.
30. Howard, L.R., Javadi, A.H., Yu, Y., Mill, R.D., Morrison, L.C., Knight, R., Loftus, M.M., Staskute, L., and Spiers, H.J. (2014). The hippocampus and entorhinal cortex encode the path and Euclidean distances to goals during navigation. Current Biology *24*, 1331-1340.
31. Garvert, M.M., Saanum, T., Schulz, E., Schuck, N.W., and Doeller, C.F. (2023). Hippocampal spatio-predictive cognitive maps adaptively guide reward generalization. Nature Neuroscience *26*, 615-626.
32. Hayes, A.F., and Rockwood, N.J. (2017). Regression-based statistical mediation and moderation analysis in clinical research: Observations, recommendations, and implementation. Behaviour research and therapy *98*, 39-57.
33. Dale, A.M., Fischl, B., and Sereno, M.I. (1999). Cortical surface-based analysis: I. Segmentation and surface reconstruction. Neuroimage *9*, 179-194.
34. Fischl, B., and Dale, A.M. (2000). Measuring the thickness of the human cerebral cortex from magnetic resonance images. Proceedings of the National Academy of Sciences *97*, 11050-11055.
35. Desikan, R.S., Ségonne, F., Fischl, B., Quinn, B.T., Dickerson, B.C., Blacker, D., Buckner, R.L., Dale, A.M., Maguire, R.P., and Hyman, B.T. (2006). An automated labeling system for subdividing the human cerebral cortex on MRI scans into gyral based regions of interest. Neuroimage *31*, 968-980.
36. Basser, P.J., and Pierpaoli, C. (2011). Microstructural and physiological features of tissues elucidated by quantitative-diffusion-tensor MRI. Journal of magnetic resonance *213*, 560-570.
37. Raven, J.C. (1938). Raven standard progressive matrices. Journal of Cognition and Development.

38. Zhang, H. (2009). The Revision of WISC-IV Chinese Version. Psychological Science *32*, 1177-1179.
39. Härdle, W.K., Simar, L., Härdle, W.K., and Simar, L. (2015). Canonical correlation analysis. Applied multivariate statistical analysis, 443-454.
40. Smith, S.M., Nichols, T.E., Vidaurre, D., Winkler, A.M., Behrens, T.E., Glasser, M.F., Ugurbil, K., Barch, D.M., Van Essen, D.C., and Miller, K.L. (2015). A positive-negative mode of population covariation links brain connectivity, demographics and behavior. Nature neuroscience *18*, 1565-1567.
41. Bush, D., Barry, C., Manson, D., and Burgess, N. (2015). Using grid cells for navigation. Neuron *87*, 507-520.
42. Whittington, J.C., Muller, T.H., Mark, S., Chen, G., Barry, C., Burgess, N., and Behrens, T.E. (2020). The Tolman-Eichenbaum machine: unifying space and relational memory through generalization in the hippocampal formation. Cell *183*, 1249-1263. e1223.
43. Butler, W.N., Hardcastle, K., and Giocomo, L.M. (2019). Remembered reward locations restructure entorhinal spatial maps. Science *363*, 1447-1452.
44. Boccara, C.N., Nardin, M., Stella, F., O'Neill, J., and Csicsvari, J. (2019). The entorhinal cognitive map is attracted to goals. Science *363*, 1443-1447.
45. Spelke, E.S., and Kinzler, K.D. (2007). Core knowledge. Developmental science *10*, 89-96.
46. Izard, V., Pica, P., Dehaene, S., Hinchey, D., and Spelke, E. (2011). Geometry as a universal mental construction. In Space, time and number in the brain, (Elsevier), pp. 319-332.
47. Gouteux, S., and Spelke, E.S. (2001). Children's use of geometry and landmarks to reorient in an open space. Cognition *81*, 119-148.
48. Schlichting, M.L., and Preston, A.R. (2015). Memory integration: neural mechanisms and implications for behavior. Current opinion in behavioral sciences *1*, 1-8.
49. Schlichting, M.L., Guarino, K.F., Roome, H.E., and Preston, A.R. (2022). Developmental differences in memory reactivation relate to encoding and inference in the human brain. Nature human behaviour *6*, 415-428.
50. Shepard, R.N. (1987). Toward a universal law of generalization for psychological science. Science *237*, 1317-1323.
51. Shepard, R.N. (1994). Perceptual-cognitive universals as reflections of the world. Psychonomic Bulletin & Review *1*, 2-28.
52. Liu, Y., Dolan, R.J., Kurth-Nelson, Z., and Behrens, T.E. (2019). Human replay spontaneously reorganizes experience. Cell *178*, 640-652. e614.
53. Nour, M.M., Liu, Y., Arumuham, A., Kurth-Nelson, Z., and Dolan, R.J. (2021). Impaired neural replay of inferred relationships in schizophrenia. Cell *184*, 4315-4328. e4317.
54. Van Kesteren, M.T., Ruiter, D.J., Fernández, G., and Henson, R.N. (2012). How schema and novelty augment memory formation. Trends in neurosciences *35*, 211-219.
55. He, Q., and Brown, T.I. (2019). Environmental Barriers Disrupt Grid-like Representations in Humans during Navigation. Curr Biol *29*, 2718-2722.e2713. 10.1016/j.cub.2019.06.072.
56. Mills, K.L., Goddings, A.-L., Clasen, L.S., Giedd, J.N., and Blakemore, S.-J. (2014). The developmental mismatch in structural brain maturation during adolescence. Developmental neuroscience *36*, 147-160.
57. Blakemore, S.-J. (2008). The social brain in adolescence. Nature Reviews Neuroscience *9*, 267-277.

58. Blakemore, S.-J., and Robbins, T.W. (2012). Decision-making in the adolescent brain. Nature neuroscience *15*, 1184-1191.
59. Mills, K.L., Goddings, A.-L., Herting, M.M., Meuwese, R., Blakemore, S.-J., Crone, E.A., Dahl, R.E., Güroğlu, B., Raznahan, A., and Sowell, E.R. (2016). Structural brain development between childhood and adulthood: Convergence across four longitudinal samples. Neuroimage *141*, 273-281.
60. Genc, S., Raven, E.P., Drakesmith, M., Blakemore, S.-J., and Jones, D.K. (2023). Novel insights into axon diameter and myelin content in late childhood and adolescence. Cerebral Cortex *33*, 6435-6448.
61. Bubb, E.J., Metzler-Baddeley, C., and Aggleton, J.P. (2018). The cingulum bundle: anatomy, function, and dysfunction. Neuroscience & Biobehavioral Reviews *92*, 104-127.
62. Dumontheil, I., Apperly, I.A., and Blakemore, S.J. (2010). Online usage of theory of mind continues to develop in late adolescence. Developmental science *13*, 331-338.
63. Rakoczy, H. (2022). Foundations of theory of mind and its development in early childhood. Nature Reviews Psychology *1*, 223-235.
64. Blakemore, S.-J. (2012). Imaging brain development: the adolescent brain. Neuroimage *61*, 397-406.
65. Blakemore, S.-J., and Frith, U. (2005). The learning brain: Lessons for education (Blackwell publishing).
66. Varga, N.L., Stewart, R.A., and Bauer, P.J. (2016). Integrating across episodes: Investigating the long-term accessibility of self-derived knowledge in 4-year-old children. J Exp Child Psychol *145*, 48-63. 10.1016/j.jecp.2015.11.015.
67. Esposito, A.G., and Bauer, P.J. (2017). Going beyond the lesson: Self-generating new factual knowledge in the classroom. J Exp Child Psychol *153*, 110-125. 10.1016/j.jecp.2016.09.003.
68. Weiskopf, N., Hutton, C., Josephs, O., and Deichmann, R. (2006). Optimal EPI parameters for reduction of susceptibility-induced BOLD sensitivity losses: a whole-brain analysis at 3 T and 1.5 T. Neuroimage *33*, 493-504.
69. Esteban, O., Markiewicz, C.J., Blair, R.W., Moodie, C.A., Isik, A.I., Erramuzpe, A., Kent, J.D., Goncalves, M., DuPre, E., and Snyder, M. (2019). fMRIPrep: a robust preprocessing pipeline for functional MRI. Nature methods *16*, 111-116.
70. Gorgolewski, K., Burns, C.D., Madison, C., Clark, D., Halchenko, Y.O., Waskom, M.L., and Ghosh, S.S. (2011). Nipype: a flexible, lightweight and extensible neuroimaging data processing framework in python. Frontiers in neuroinformatics *5*, 13.
71. Tustison, N.J., Avants, B.B., Cook, P.A., Zheng, Y., Egan, A., Yushkevich, P.A., and Gee, J.C. (2010). N4ITK: improved N3 bias correction. IEEE transactions on medical imaging *29*, 1310-1320.
72. Avants, B.B., Epstein, C.L., Grossman, M., and Gee, J.C. (2008). Symmetric diffeomorphic image registration with cross-correlation: evaluating automated labeling of elderly and neurodegenerative brain. Medical image analysis *12*, 26-41.
73. Zhang, Y., Brady, M., and Smith, S. (2001). Segmentation of brain MR images through a hidden Markov random field model and the expectation-maximization algorithm. IEEE transactions on medical imaging *20*, 45-57.
74. Fonov, V.S., Evans, A.C., McKinstry, R.C., Almli, C.R., and Collins, D. (2009). Unbiased nonlinear average age-appropriate brain templates from birth to adulthood. NeuroImage *47*, S102.
75. Huntenburg, J.M. (2014). Evaluating nonlinear coregistration of BOLD EPI and T1w images. (Freie Universität Berlin).

76. Wang, S., Peterson, D.J., Gatenby, J.C., Li, W., Grabowski, T.J., and Madhyastha, T.M. (2017). Evaluation of field map and nonlinear registration methods for correction of susceptibility artifacts in diffusion MRI. Frontiers in neuroinformatics *11*, 17.
77. Treiber, J.M., White, N.S., Steed, T.C., Bartsch, H., Holland, D., Farid, N., McDonald, C.R., Carter, B.S., Dale, A.M., and Chen, C.C. (2016). Characterization and correction of geometric distortions in 814 diffusion weighted images. PloS one *11*, e0152472.
78. Jenkinson, M., and Smith, S. (2001). A global optimisation method for robust affine registration of brain images. Medical image analysis *5*, 143-156.
79. Greve, D.N., and Fischl, B. (2009). Accurate and robust brain image alignment using boundary-based registration. Neuroimage *48*, 63-72.
80. Jenkinson, M., Bannister, P., Brady, M., and Smith, S. (2002). Improved optimization for the robust and accurate linear registration and motion correction of brain images. Neuroimage *17*, 825-841.
81. Cox, R.W., and Hyde, J.S. (1997). Software tools for analysis and visualization of fMRI data. NMR in Biomedicine: An International Journal Devoted to the Development and Application of Magnetic Resonance In Vivo *10*, 171-178.
82. Lanczos, C. (1964). Evaluation of noisy data. Journal of the Society for Industrial and Applied Mathematics, Series B: Numerical Analysis *1*, 76-85.
83. Cieslak, M., Cook, P.A., He, X., Yeh, F.-C., Dhollander, T., Adebimpe, A., Aguirre, G.K., Bassett, D.S., Betzel, R.F., and Bourque, J. (2021). QSIPrep: an integrative platform for preprocessing and reconstructing diffusion MRI data. Nature methods *18*, 775-778.
84. Veraart, J., Novikov, D.S., Christiaens, D., Ades-Aron, B., Sijbers, J., and Fieremans, E. (2016). Denoising of diffusion MRI using random matrix theory. Neuroimage *142*, 394-406.
85. Andersson, J.L., and Sotiropoulos, S.N. (2016). An integrated approach to correction for off-resonance effects and subject movement in diffusion MR imaging. Neuroimage *125*, 1063-1078.
86. Andersson, J.L., Graham, M.S., Zsoldos, E., and Sotiropoulos, S.N. (2016). Incorporating outlier detection and replacement into a non-parametric framework for movement and distortion correction of diffusion MR images. Neuroimage *141*, 556-572.
87. Andersson, J.L., Skare, S., and Ashburner, J. (2003). How to correct susceptibility distortions in spin-echo echo-planar images: application to diffusion tensor imaging. Neuroimage *20*, 870-888.
88. Jenkinson, M., and Woolrich, M. (2000). Asymptotic T to Z and F to Z statistic transformations. Internal Technical Report TR00MJ1, Oxford Centre for Functional Magnetic ….
89. Kriegeskorte, N., Mur, M., and Bandettini, P.A. (2008). Representational similarity analysis-connecting the branches of systems neuroscience. Frontiers in systems neuroscience, 4.
90. Barron, H.C., Garvert, M.M., and Behrens, T.E. (2016). Repetition suppression: a means to index neural representations using BOLD? Philosophical Transactions of the Royal Society B: Biological Sciences *371*, 20150355.
91. Smith, R., Skoch, A., Bajada, C.J., Caspers, S., and Connelly, A. (2020). Hybrid surface-volume segmentation for improved anatomically-constrained tractography.
92. Dhollander, T., Raffelt, D., and Connelly, A. (2016). Unsupervised 3-tissue response function estimation from single-shell or multi-shell diffusion MR data without a co-registered T1 image. In 5. (Lisbon, Portugal).

93. Tournier, J.-D., Calamante, F., Gadian, D.G., and Connelly, A. (2004). Direct estimation of the fiber orientation density function from diffusion-weighted MRI data using spherical deconvolution. Neuroimage *23*, 1176-1185.
94. Tournier, J.-D., Yeh, C.-H., Calamante, F., Cho, K.-H., Connelly, A., and Lin, C.-P. (2008). Resolving crossing fibres using constrained spherical deconvolution: validation using diffusion-weighted imaging phantom data. Neuroimage *42*, 617-625.
95. Dhollander, T., Mito, R., Raffelt, D., and Connelly, A. (2019). Improved white matter response function estimation for 3-tissue constrained spherical deconvolution. In 10.
96. Raffelt, D., Dhollander, T., Tournier, J.-D., Tabbara, R., Smith, R.E., Pierre, E., and Connelly, A. (2017). Bias field correction and intensity normalisation for quantitative analysis of apparent fibre density. pp. 3541.
97. Tournier, J.-D., Smith, R., Raffelt, D., Tabbara, R., Dhollander, T., Pietsch, M., Christiaens, D., Jeurissen, B., Yeh, C.-H., and Connelly, A. (2019). MRtrix3: A fast, flexible and open software framework for medical image processing and visualisation. Neuroimage *202*, 116137.
98. Smith, R.E., Tournier, J.-D., Calamante, F., and Connelly, A. (2012). Anatomically-constrained tractography: improved diffusion MRI streamlines tractography through effective use of anatomical information. Neuroimage *62*, 1924-1938.
99. Smith, R.E., Tournier, J.-D., Calamante, F., and Connelly, A. (2015). SIFT2: Enabling dense quantitative assessment of brain white matter connectivity using streamlines tractography. Neuroimage *119*, 338-351.
100. Beaulieu, C. (2002). The basis of anisotropic water diffusion in the nervous system–a technical review. NMR in Biomedicine: An International Journal Devoted to the Development and Application of Magnetic Resonance In Vivo *15*, 435-455.
101. Maffei, C., Lee, C., Planich, M., Ramprasad, M., Ravi, N., Trainor, D., Urban, Z., Kim, M., Jones, R., and Henin, A. (2021). Using diffusion MRI data acquired with ultra-high gradient strength to improve tractography in routine-quality data. Neuroimage *245*, 118706.
102. Wang, S., Tepfer, L.J., Taren, A.A., and Smith, D.V. (2020). Functional parcellation of the default mode network: a large-scale meta-analysis. Scientific Reports *10*, 16096.
103. Vallat, R. (2018). Pingouin: statistics in Python. J. Open Source Softw. *3*, 1026.
104. Smith, S.M., Jenkinson, M., Woolrich, M.W., Beckmann, C.F., Behrens, T.E., Johansen-Berg, H., Bannister, P.R., De Luca, M., Drobnjak, I., and Flitney, D.E. (2004). Advances in functional and structural MR image analysis and implementation as FSL. Neuroimage *23*, S208-S219.

Extended Data Figures

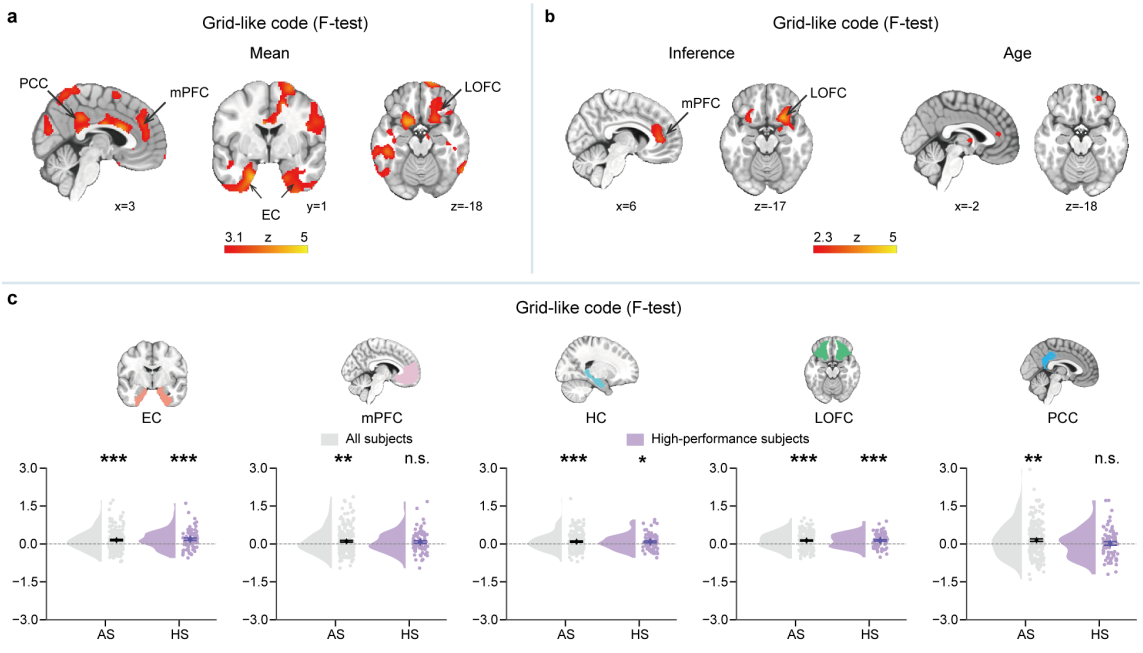

Extended Data Fig. 1 | Grid-like code for inferred trajectories. a, Grid-like code was identified using the z-transform F statistic. Whole-brain analysis displayed grid-like code in brain regions, including EC, mPFC, LOFC, PCC and precentral gyrus (also see **Supplementary Table 1**). The brain maps survived whole-brain FWE corrected at the cluster level ($p < 0.05$) with a cluster-forming voxel threshold of $p < 0.01$. **b,** The whole-brain covariate maps show that the mPFC and LOFC exhibit positive correlations between the grid-like code and the ability of inferential reasoning. However, corresponding areas have only shown a feeble age effect. The covariate maps were thresholded at $p < 0.01$, uncorrected, for visualization purpose. **c,** ROI analysis of grid-like code (F-test). The top row shows the ROIs, which were independently defined from previous studies. The second row shows the mean activity of grid-like code within the corresponding ROIs for all subjects (AS, grey) and high-performance subjects (HS, purple). Significance is denoted as: * $p < 0.05$. ** $p < 0.01$. *** $p < 0.001$. n.s. non-significant.

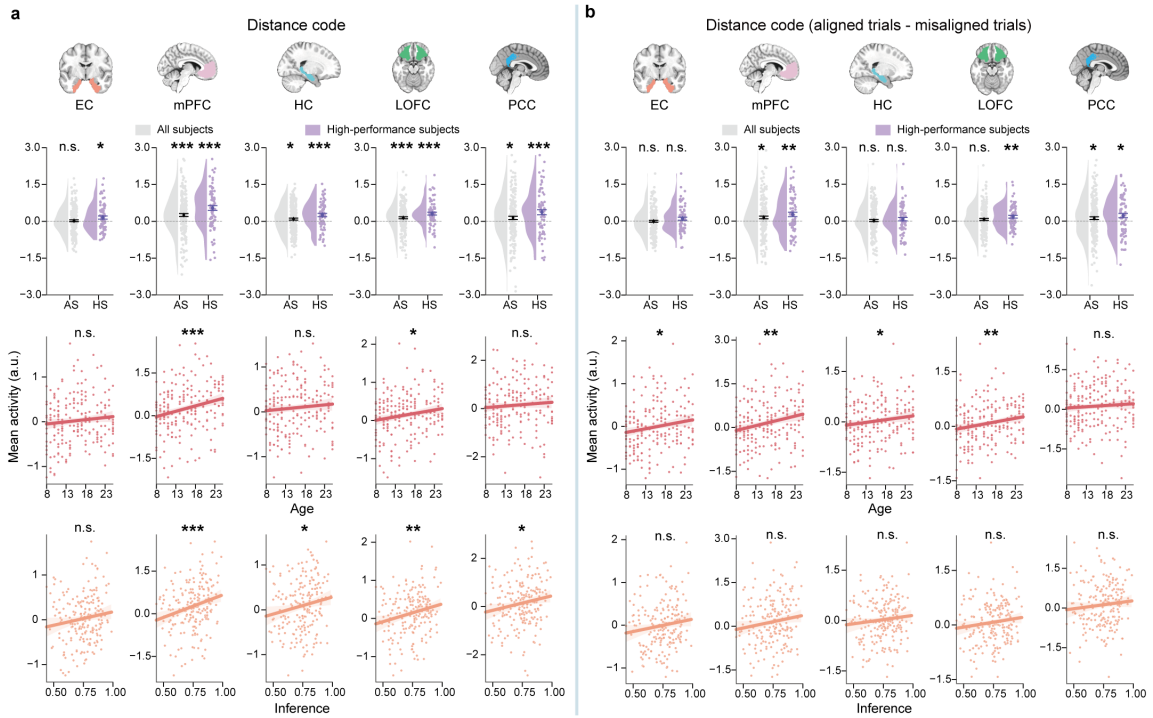

Extended Data Fig. 2 | ROI analysis related to distance code in Game1. a, ROI analysis of distance code. The top row shows the ROIs, which were independently defined from previous studies. The second row shows the mean activity of distance code within the corresponding ROIs for all subjects (AS, grey) and high-performance subjects (HS, purple). The third row shows the correlations between age and the distance code within the ROIs. The fourth row shows the correlations between inference performance and the distance code within the ROIs. **b,** ROI analysis for grid-like modulation on distance code. This involves contrasting the distance code of aligned and misaligned trials within ROIs. The trials were labelled based on whether the inferred direction aligned or misaligned with the estimated mean orientation from EC. The layout mirrors panel A. Significance is denoted as: * $p < 0.05$. ** $p < 0.01$. *** $p < 0.001$. n.s. non-significant.

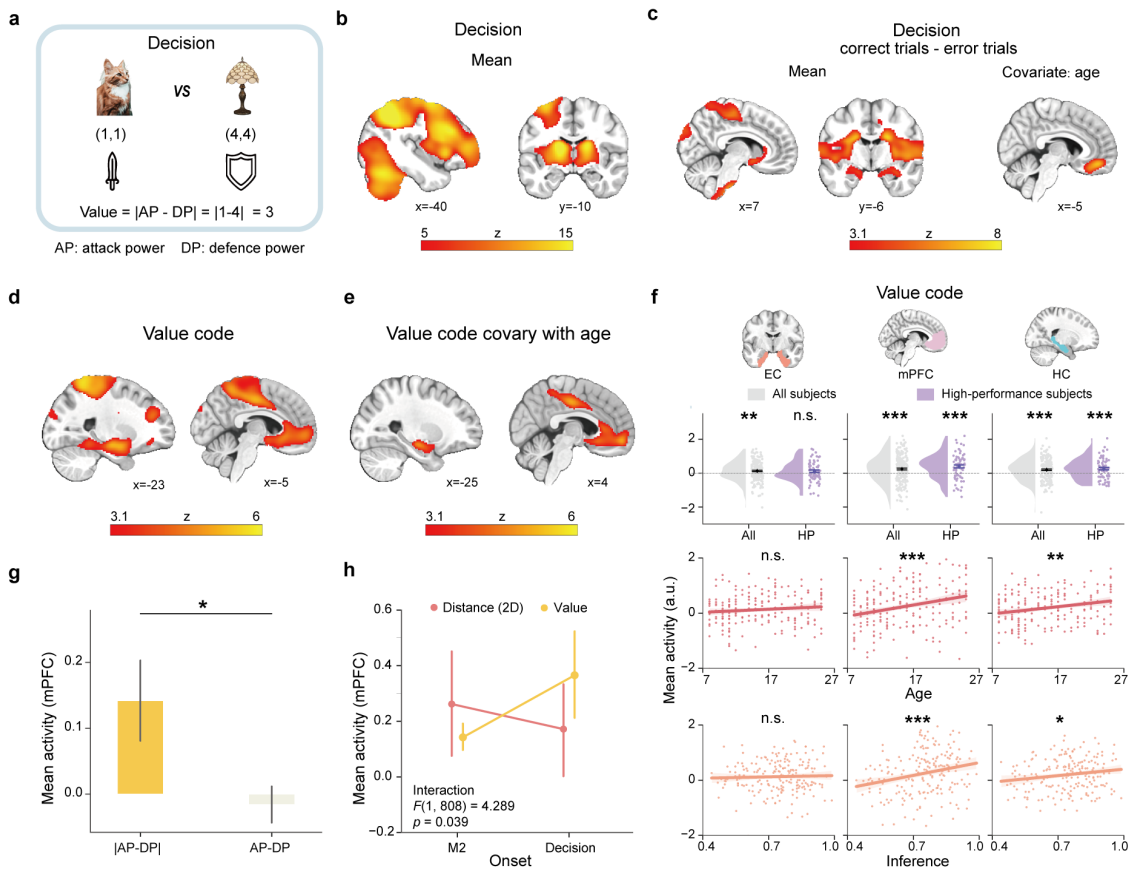

Extended Data Fig. 3 | Value code at decision. a, A trial demonstration illustrates how the value code was calculated. We compared the AP of attacking monsters to the DP of defending monsters and calculated the absolute difference between AP and DP as the value code. **b,** Whole-brain analysis shows the mean activity during decision time with significant activation in the cerebellum, visual cortex, striatum, primary motor cortex and dorsolateral prefrontal cortex. **c,** Contrast brain map between correct versus error response trials, showing stronger activation in ventral striatum, amygdala and primary motor cortex. The covariate results (right panel) show that the difference between correct trials and error trials increase with age in the mPFC. **d,** Whole-brain parametric analysis with value code found significant involvement of hippocampus, mPFC, and primary motor cortex. **e,** Whole-brain covariate analysis with age for value code. **f**. ROI analysis of value code. The top row shows the ROIs. The second row shows the mean activity of value code within the corresponding ROIs for all subjects (AS, grey) and high-performance subjects (HS, purple). The third row shows the correlations between age and the value code within the ROIs. The fourth row shows the correlations with inference performance. **g.** ROI analysis shows that the value code in mPFC represents the absolute difference between AP and DP, rather than the difference between AP and DP (|AP-DP|: $t(202) = 2.33$, $p = 0.02$; AP-DP: $t(202) = -0.58$, $p = 0.56$; one-sample t-test). **h.** A shift in neural representation within the mPFC, from representing the distance code at M2 stage to encoding the value code during the decision time. All brain maps survived whole-brain FWE corrected at the cluster level ($p < 0.05$) with a cluster-forming voxel threshold of $p < 0.001$. Significance is denoted as: * $p < 0.05$. ** $p < 0.01$. *** $p < 0.001$. n.s. non-significant.

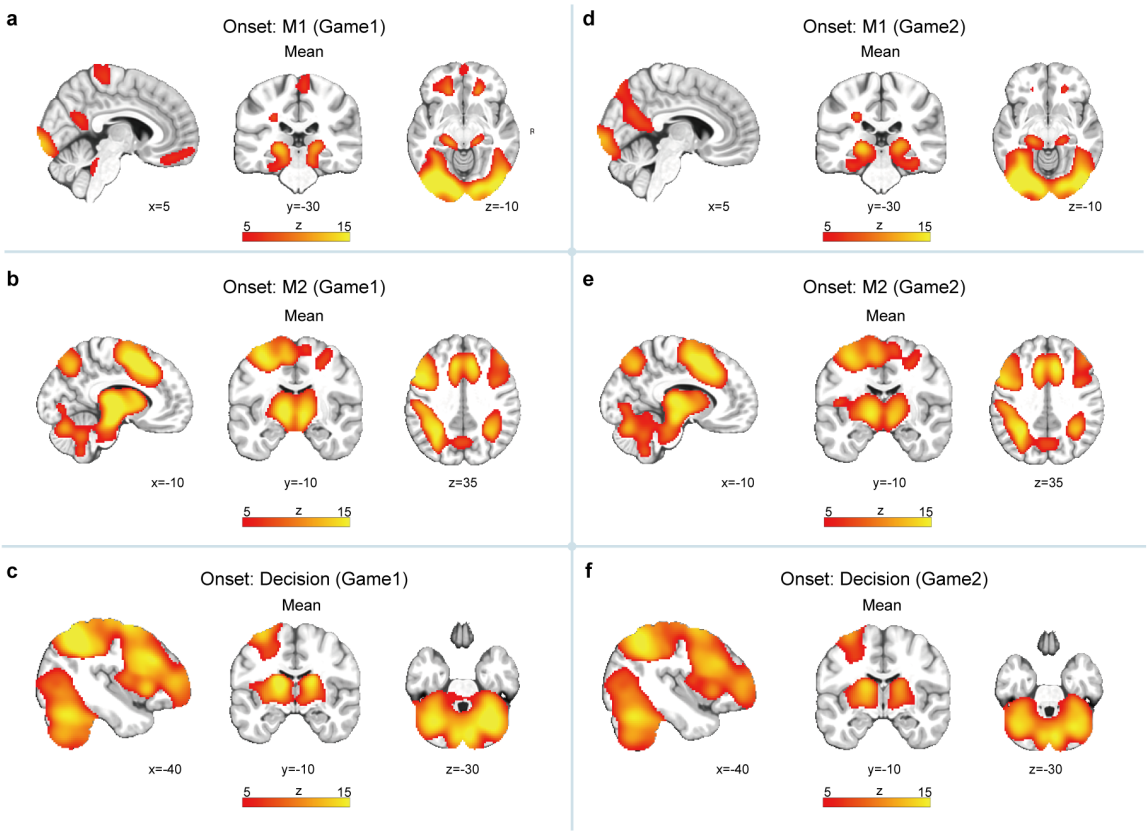

Extended Data Fig. 4 | Mean activity during different phases of an inference trial in both Game1 and Game2. a, At the onset of M1 (Game1), whole-brain analysis revealed significant activations in visual cortex, posterior cingulate cortex, and posterior hippocampus. **b,** At the onset of M2 (Game1), significant activations were found in anterior cingulate cortex, visual cortex, and superior parietal lobule. **c,** Upon decision time (Game1), we observed significant activation in the cerebellum, visual cortex, striatum, primary motor cortex and dorsolateral prefrontal cortex. **d-f,** In Game2, whole-brain analysis revealed similar activation patterns across each phase. All brain maps were whole-brain FWE corrected at the cluster level ($p < 0.05$) with a cluster-forming voxel threshold of $p < 0.001$. For visualization purpose, whole-brain maps presented here were thresholded at z-value > 5.

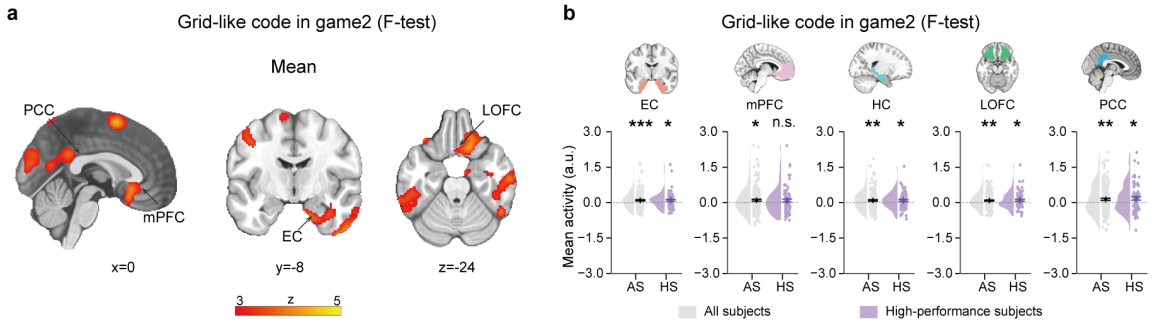

Extended Data Fig. 5 | Grid-like code for inferred trajectories in Game2 a, Whole-brain results are displayed, showing the clusters exhibiting grid-like code (*F*-test) of Game2. The clusters include the EC, OFC, PCC (also see **Supplementary Table 4**). This map survived whole-brain FWE correction at the cluster level ($p < 0.05$) with a cluster-forming voxel threshold of $p < 0.01$. **b,** ROI results of grid-like code (*F*-test) in Game2. The top row shows the ROIs, which were independently defined from previous studies. The second row shows the mean activity of grid-like code within the corresponding ROIs for all subjects (AS, grey) and high-performance subjects (HS, purple). Significance is denoted as: * $p < 0.05$. ** $p < 0.01$. *** $p < 0.001$. n.s. non-significant.

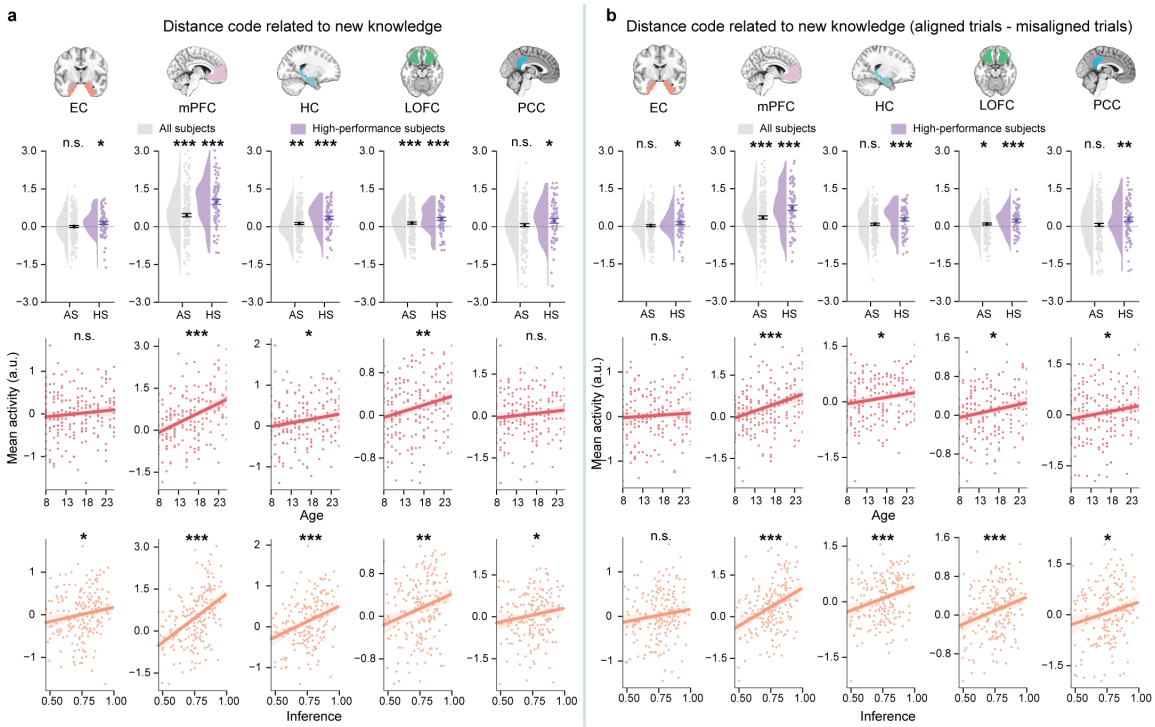

Extended Data Fig. 6 | Distance code related to new knowledge a, ROI analysis of distance code related to new knowledge. The top row shows the ROIs, which were independently defined from previous studies. The second row shows the mean activity of distance code within the corresponding ROIs for all subjects (AS, grey) and high-performance subjects (HS, purple). The third row shows the correlations between the distance code within ROI and age (red). The fourth row shows the correlations with inference performance of Game2 (orange). **b,** ROI analysis for grid-like modulation on distance code related to new knowledge. The layout mirrors panel A. Notably, we split these trials according to the mean orientation estimated from EC in Game1. Significance is denoted as: * $p < 0.05$. ** $p < 0.01$. *** $p < 0.001$. n.s. non-significant.

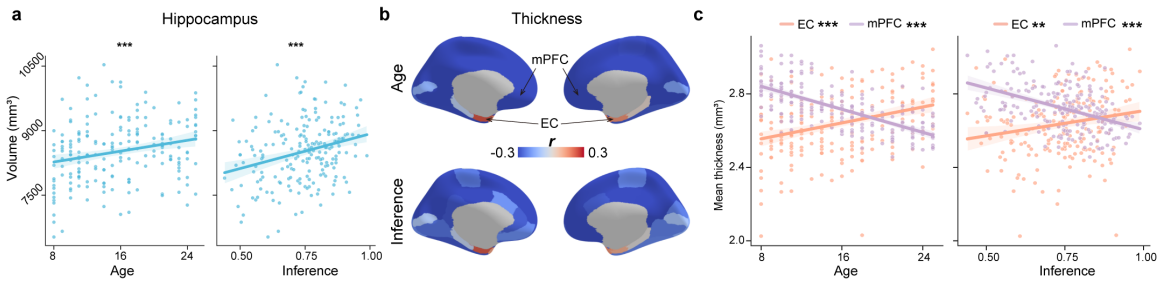

Extended Data Fig. 7 | The structural development of the hippocampus and measures of grey matter thickness in the cortex. a, Developmental trajectory of hippocampal volume. ROI analysis depicted that the hippocampal volume showed significant positive correlations with age and inferential reasoning ability. **b,** Regional correlations between cortical thickness and both age (top panel) and inference ability (bottom panel) for each of the 34 bilateral brain regions defined by the Desikan–Killiany parcellation [35]. Like GMV, the EC cortical thickness increases in tandem with age and inference ability from 8 to 25 years old, contrasting with the decreasing trend in most other regions. **c,** ROI analysis of cortical thickness in the bilateral EC and mPFC, highlighting the divergent developmental patterns in the EC (coral) and mPFC (purple) on cortical thickness. Each dot represents data from an individual subject. **: $p < 0.01$. ***: $p < 0.001$.

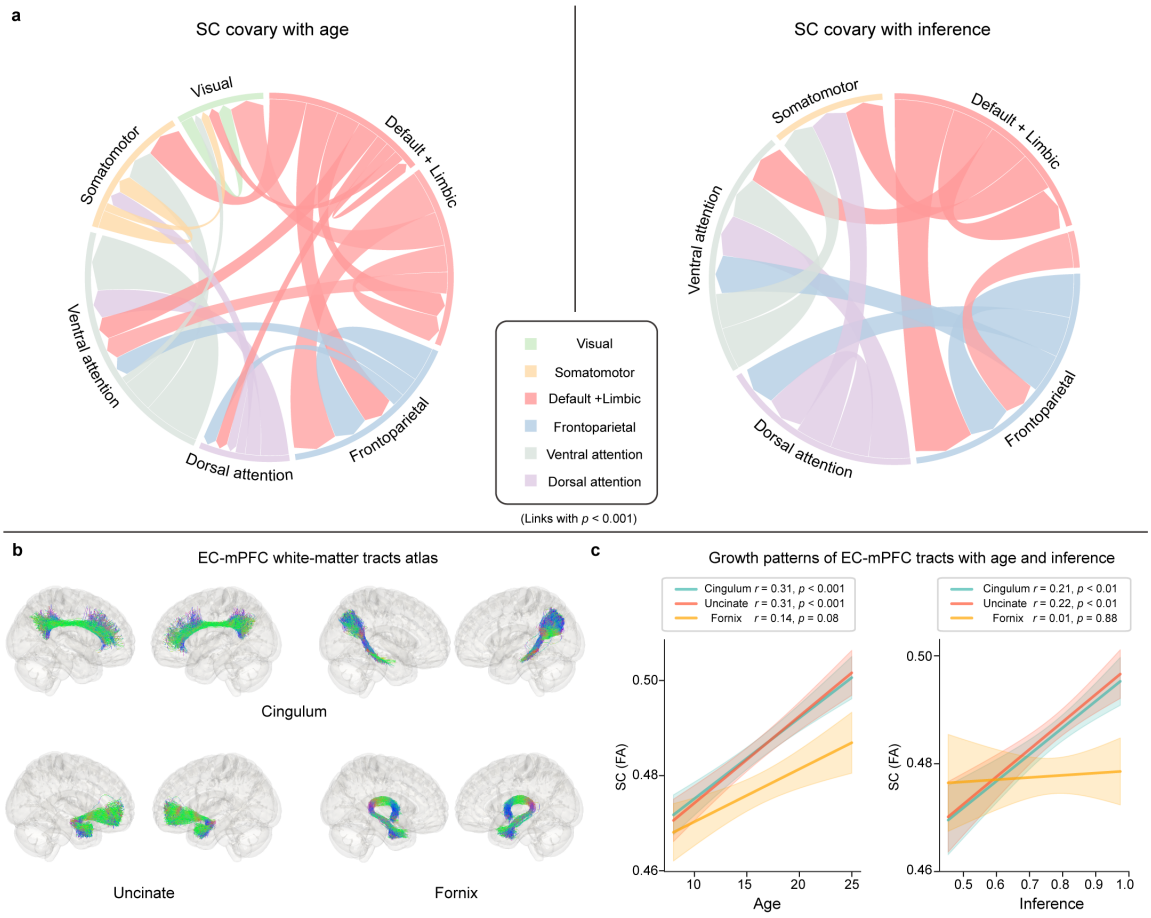

Extended Data Fig. 8 | Changes in structural connectivity across brain networks related to age and inferential performance. a, The chord diagram illustrates changes in structural connectivity (measured by FA) associated with age and inference performance, based on 7 brain networks identified by Yeo et al. (2011). Each link represents the correlation between structural connectivity and either age or inferential performance, with the line thickness indicating the relative strength of structural connectivity among the networks. Notably, the default mode and limbic networks, which include the brain regions of interest (ROI), i.e., MTL-mPFC, show a stronger positive correlation with inference performance compared to the visual and somatomotor networks. Only links demonstrating significant correlations ($p < 0.001$) are displayed. **b,** Three canonical white-matter tracts connecting the MTL and PFC are labelled using an independent dataset by Maffei *et al.* [101]. These tracts, namely the cingulum, uncinate, and fornix, are used as masks for subsequent analyses. **c,** All white-matter tracts connecting the EC and mPFC exhibited a positive trend with age. However, significant correlations with inferential performance were observed only in the changes of the cingulum and uncinate.

Extended Data Tables

Extended Data Table 1 | Demographic information of subjects.

Characteristics	Subjects	
	Age 8-16	Age 17-25
N	116	87
Age (SD) in years	11.66 (2.55)	20.94 (2.83)
Female (%)	48.28	67.82
Mean SPM score (SD)	51.91 (5.88)	--
WISC-IV		
Coding	67.85 (22.44)	--
Digit Span	28.27 (5.12)	--
Verbal Similarities	33.6 (3.93)	--
Verbal Comprehension	29.32 (6.02)	--
Perceptual Matrix	28.52 (3.92)	--
Perceptual Block	53.24 (10.46)	--

SPM, Raven's Standard Progressive Matrices; WISC-IV, Wechsler Intelligence Scale for Children - Fourth Edition. --, not applicable.